

AD-A210 134

FILE COPY

AFOSR-TR-89-0778

2

**LASER CLADDING OF NI, Nb, AND Mg ALLOYS
FOR IMPROVED ENVIRONMENTAL
RESISTANCE AT HIGH TEMPERATURE**

**Final Report
for Research Conducted through the Period
November 1985 through October 1988
under**

**Contract No. AFOSR 85-0333
Submitted to
Air Force Office of Scientific Research
Building 410**

**ATTN: Dr. A. Rosenstein
Bolling Air Force Base
Washington, DC 20332**

**SDTIC
ELECTE
JUL 05 1989**

@b H

Prepared by

**J. Mazumder, S. Sircar, A. Kar,
C. Ribaudo, R. Lober, and R. Subramanian**

Chief, Technical Information Division

AFOSR-TR-89-0778



**Laser Aided Materials Processing Laboratory
Department of Mechanical and Industrial Engineering
University of Illinois at Urbana-Champaign
1206 West Green Street
Urbana, IL 61801**

DISTRIBUTION STATEMENT A

**Approved for public release;
Distribution Unlimited**

89 6 29 030

UNCL.

SECURITY CLASSIFICATION OF THIS PAGE

REPORT DOCUMENTATION PAGE				Form Approved OMB No. 0704-0188	
1a. REPORT SECURITY CLASSIFICATION UNCL.			1b. RESTRICTIVE MARKINGS		
2a. SECURITY CLASSIFICATION AUTHORITY			3. DISTRIBUTION / AVAILABILITY OF REPORT Approved for public release, distribution unlimited UNLIMITED		
2b. DECLASSIFICATION / DOWNGRADING SCHEDULE					
4. PERFORMING ORGANIZATION REPORT NUMBER(S)			5. MONITORING ORGANIZATION REPORT NUMBER(S) AFOSR-TR-89-0778		
6a. NAME OF PERFORMING ORGANIZATION UNIV. OF ILL.		6b. OFFICE SYMBOL (if applicable) MECH. ENGR.		7a. NAME OF MONITORING ORGANIZATION AFOSR/NE	
6c. ADDRESS (City, State, and ZIP Code) URBANA, ILL. 61801		7b. ADDRESS (City, State, and ZIP Code) BLDG. 410 BOLLING AFB, DC. 20332-6448			
8a. NAME OF FUNDING / SPONSORING ORGANIZATION AFOSR		8b. OFFICE SYMBOL (if applicable) NE		9. PROCUREMENT INSTRUMENT IDENTIFICATION NUMBER AFOSR-85-0333	
8c. ADDRESS (City, State, and ZIP Code) BOLLING, AFB, D.C. 20332		10. SOURCE OF FUNDING NUMBERS			
		PROGRAM ELEMENT NO. 61102F	PROJECT NO. 2306	TASK NO. A1	WORK UNIT ACCESSION NO. —
11. TITLE (Include Security Classification) (U) LASER CLADDING OF Ni, Nb + Mg Alloys					
12. PERSONAL AUTHOR(S) J. MAZUMDER ET AL.					
13a. TYPE OF REPORT FINAL		13b. TIME COVERED FROM 11/85 TO 10/88		14. DATE OF REPORT (Year, Month, Day) JUNE 1989	
15. PAGE COUNT 52					
16. SUPPLEMENTARY NOTATION					
17. COSATI CODES			18. SUBJECT TERMS (Continue on reverse if necessary and identify by block number)		
FIELD	GROL	SUB-GROUP			
11.06			LASER CLADDING		
			Ni Alloys		
			Nb Alloys		
			Mg Alloys		
			Environmental Resistance		
19. ABSTRACT (This report summarizes experimental and theoretical studies carried out during the period of November 1985 to October 1988 on laser surface modification of Ni, Nb and Mg alloys for improved environmental resistance at high temperature. Major emphasis has been on Ni-Cr-Al-Hf system. Microstructural evolution and oxidation properties of Ni and Nb alloys were examined. For Mg alloys microstructural characterization and potentiodynamic corrosion testing were carried out. One-dimensional diffusion model for finite domain to examine the extended solid solubility in laser cladding was also developed. JES)					
20. DISTRIBUTION / AVAILABILITY OF ABSTRACT <input checked="" type="checkbox"/> UNCLASSIFIED/UNLIMITED <input type="checkbox"/> SAME AS RPT. <input type="checkbox"/> DTIC USERS			21. ABSTRACT SECURITY CLASSIFICATION UNCL.		
22a. NAME OF RESPONSIBLE INDIVIDUAL A. H. Kozanstein			22b. TELEPHONE (Include Area Code) (202) 267-4933		22c. OFFICE SYMBOL AFOSR/NE

UNCL.

TABLE OF CONTENTS

	Page
EXECUTIVE SUMMARY	iii
1. INTRODUCTION	1
2. LASER CLADDING OF NICKEL-Cr-Al-Hf SYSTEM	3
2.1 Microstructure Evolution	3
2.1.1 Experimental Procedure	3
2.1.2 Results and Discussion	6
2.2 Oxidation Properties	8
2.2.1 Experimental Procedure	9
2.2.2 Results and Discussion	9
2.3 Conclusion	15
2.4 Future Work	16
3. LASER CLADDING OF Nb-Ti SYSTEM	17
3.1 Experimental Procedure	17
3.2 Results and Discussion	17
3.3 Conclusion	22
3.4 Future Work	22
4. CORROSION RESISTANCE PROPERTIES OF LASER CLAD Mg-Zr SYSTEM	24
4.1 Experimental Procedure	24
4.2 Results and Discussion	25
4.3 Conclusions	35
4.4 Future Work	37
5. SPECTROSCOPIC STUDIES	40
5.1 Temperature Measurement	40
5.1.1 Experimental Procedure	40
5.1.2 Results and Discussion	40
5.2 Future Work: Concentration Measurement	46
6. MATHEMATICAL MODELING OF EXTENDED SOLID SOLUTION IN LASER CLADDING	48
6.1 Current Work	48
6.2 Future Work	53
7. REFERENCES	54
APPENDIX A: PUBLICATION LIST	57

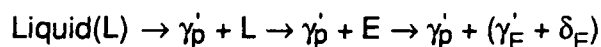
EXECUTIVE SUMMARY

The technique of laser surface modification provides a unique means of synthesizing novel nonequilibrium materials in near net shape. Environmental resistance of nickel, magnesium and niobium alloys can be improved by means of this laser based technique. The advantage of laser surface modification technique is enormous savings of alloying elements, which are often expensive or strategically important, can be achieved. This is possible since only the surface is being modified. Also, components with rapidly solidified structure can be made in near net shape by building multiple layers by laser cladding whereas the other rapid solidification techniques (RST) requires consolidation process where temperature and pressure cycle induce phase transition in metastable phases.

The goal of this program is to develop a science base for synthesis of nonequilibrium metastable alloys by laser processing. The specific objectives are: 1) to develop fundamental understanding of the mechanism of formation of metastable phases involving extended solid solution and amorphous phase, 2) to study the effect of metastable crystalline and amorphous structure on a) the high temperature oxidation properties of laser clad Ni and Nb alloys, and b) the corrosion properties of laser clad Mg alloys, and 3) to develop the correlation between process parameters, microstructure and oxidation/corrosion properties of the above alloys.

This report summarizes experimental and theoretical studies carried out during the period of November 1985 to October 1988 on laser surface modification of Ni, Nb and Mg alloys for improved environmental resistance at high temperature. Major emphasis has been on Ni-Cr-Al-Hf system. Microstructural evolution and oxidation properties of Ni and Nb alloys were examined. For Mg alloys microstructural characterization and potentiodynamic corrosion testing were carried out. One-dimensional diffusion model for finite domain to examine the extended solid solubility in laser cladding was also developed.

Laser cladding of Ni-Cr-Al-Hf for various compositions were carried out including one close to stoichiometric Ni₃Al with chromium and Hf. Microstructure of these alloys were characterized using optical, scanning and transmission electron microscopic techniques. Convergent beam techniques were applied in TEM to identify small phases. X-ray analysis with SEM and TEM and Auger Spectroscopy were carried out to determine the microchemistry and crystal structure. Differential thermal analysis (DTA) was also performed to obtain the γ' dissolution temperature. Previous report discussed the microstructure evolution of Ni-Cr-Al-Hf with 58 at% Ni. This report mainly discusses the microstructure evolution for Ni-Cr-Al-Hf with 70 at% Ni (near stoichiometric Ni₃Al). The microstructure of these alloys mainly consists of dendritic zone full of γ' (Ni₃Al) and Hf rich interdendritic eutectics. Aluminum in Ni₃Al was often found to be partially replaced by Cr and Hf. Although there were some subtle differences in cell spacing, composition and other minor features between the samples depending on the process parameters but within the range of experimental parameters no radical differences were observed. Based on the observations made the possible phase transformation sequence of this group of laser clad Ni-Cr-Al-Hf are suggested below.



where γ'_p is the primary γ' phase with ordered f.c.c. structure (L1₂), γ'_E is eutectic γ' phase with ordered f.c.c. structure, E is eutectic phase and δ_E is the other eutectic phase with heavily faulted f.c.c. structure.

Antiphase boundaries (APBs), in the γ' (ordered f.c.c) phase and the effect of process parameters on their morphology was also discussed. Initial DTA work indicated that γ' -dissolution temperature is at least as high as Rene 80 if not higher. More work is needed in this area.

Codes	
A-11 and/or	
Specimen	
A-1	

Thermogravimetric analysis for the evaluation of oxidation resistance were carried out. Initial studies indicated that 58 at.% Ni+Cr+Al+Hf clad alloy lead to marginal improvement of oxidation resistance over Rene 80 whereas 70 at.% Ni Cr+Al+Hf promised far superior oxidation resistance.

Laser cladding of Ti on Nb was carried out to improve high temperature oxidation properties. The microstructure characterization revealed considerable amount of amorphous phase in this system. Also the clad region consisted of heavily faulted martensitic plates. Differential scanning calorimetry revealed the lower temperature of onset for $\alpha \rightarrow \beta$ transformation (860.2°C), indicating the extended solubility of Nb in titanium. We have also performed some cladding experiments in the Nb-Al and Nb-Al-V which are known to be high temperature oxidation resistant materials [1,2]. At 1200°C it mainly forms a passive Al_2O_3 layer. However, NbAl_3 is extremely brittle and since it is a stoichiometric line compound it is also very difficult to obtain single phase microstructure. Addition of group VB elements to NbAl_3 has been known to improve the ductility of the material. TGA results indicate that addition of V to NbAl_3 (nominal) however deteriorates the oxidation properties of NbAl_3 . Tests have been conducted with NbAl_3 (nominal) with 5, 10 and 15 at % V claddings and these results are presented in detail in this report. We have also conducted X-ray photoelectron spectroscopy studies on the oxides formed on the claddings after oxidation tests (TGA). Results indicate that addition of vanadium to NbAl_3 (nominal) reduces the tendency to form Al_2O_3 coatings on the claddings during oxidation and hence impairs the oxidation resistance of the claddings.

Laser cladding of Zr, Mg-2wt% Zr and Mg-5wt% Zr on pure magnesium were also carried out to improve the corrosion resistance of magnesium in salt water (3.5% NaCl solution). Foils prepared from the clad region of the Zr on magnesium system shows the presence of a considerable amount of amorphous phase which is present along with crystalline phases. The amorphous phase is very rich in Zr, whereas, the

crystalline phases presents in the system after laser cladding have varying amounts of magnesium and zirconium depending on the particular phase in consideration. The corrosion response of the clads show an increase in the corrosion potential as compared to pure magnesium. This has been tested via a potentiodynamic test and the results have been compared with other metals in an earlier report which revealed that Zr clad had best corrosion resistance compared to Al, Ti clad and Mg alloy ZA91B.

Microstructural studies of the claddings of Mg-2wt% Zr and Mg-5wt% Zr system show epitaxial regrowth of the clad region on the underlying pure magnesium substrate. This work also indicates that addition of zirconium to magnesium shifts the alloy towards the nobler side of the galvanic series of metals. Zirconium helps in the formation of a passivating film on the surface which prevents further attack by chloride solution. Potentiodynamic anodic polarization tests show that the anodic current density in the passivating region of the laser clad is lower than that of the commercially available alloy ZA91B.

In addition to the experimental work theoretical modeling of diffusion was also carried out to estimate the extent of the extended solid solution in laser cladding. By incorporating non-equilibrium partition coefficient for dilute solution the model was used to determine non-equilibrium phase diagram for Ni-Hf and Ni-Al systems. The theoretical prediction reasonably agreed with the experimental data. Presently, we are developing a mathematical model for non-equilibrium partition coefficient for concentrated solution which will further improve our understanding of the process.

This ongoing project has already lead to significant advancement of the science for laser synthesis of nonequilibrium alloys. This is reflected in the various publications derived out of this work. List of publications from this project is given in Appendix A.

1. INTRODUCTION

The goal of this program is to develop a science base for synthesis of nonequilibrium metastable alloys by laser processing. The specific objectives are: 1) to develop fundamental understanding of the mechanism of formation of metastable phases involving extended solid solution and amorphous phase, 2) to study the effect of metastable crystalline and amorphous structure on a) the high temperature oxidation properties of laser clad Ni and Nb alloys, and b) the corrosion properties of laser clad Mg alloys, and 3) to develop the correlation between process parameters, microstructure and oxidation /corrosion properties of the above alloys.

The approach taken is to undertake parallel theoretical and experimental effort. The theoretical effort examines the redistribution of solute during rapid solidification in laser processing by modeling the kinetics of solute at the interface. Nonequilibrium partition coefficient for concentrated solution is considered for the kinetics model. Mathematical models to determine the regimes of process parameters for producing metastable crystalline phases are developed. In the experimental work microstructure and microchemistry are determined using electron optical techniques such as transmission electron microscopy (TEM), scanning electron microscopy (SEM), Auger Electron Spectroscopy (AES), X-ray Photoelectron Spectroscopy (XPS) and Electron Probe Microanalysis (EPMA). Microdiffraction technique such as Convergent Beam Diffraction Analysis is used for identification of small submicron phases observed in laser processed materials. Oxidation behavior is mainly studied using thermogravimetric analysis technique. Corrosion behavior of magnesium alloys is studied using potentiodynamic tests. Stability of the metastable crystalline and amorphous phases is determined using Differential Scanning Calorimetric technique.

Emission spectroscopy for on-line diagnostics of the process physics is also initiated. The emission spectroscopy will provide vital information such as: 1) energy partitioning between plasma/vapor and the substrate, (i.e., fraction of energy absorbed

by the substrate compared to that by the plasma), 2) chemistry of the vapor which can be correlated to the alloy substrate chemistry, and 3) attenuation of the beam due to refraction in the plasma column.

Important results and experimental procedures are summarized in Chapters 2 through 5, which are organized based on the alloys systems considered. Theoretical treatment of the extension of solid solution density laser cladding is described in Chapter 6. Publications are listed in Appendix A are also referred when appropriate for further details.

2. LASER CLADDING OF Ni-BASED SYSTEM

2.1 Microstructural Evolution

2.1.1 Experimental Procedures

In order to achieve goals of this project, the approach we have taken can be enumerated as follows:

- (a) produce laser claddings using elemental metal powder mixtures and a 10 KW continuous wave CO₂ laser using insitu laser cladding techniques as shown in Fig. 1.
- (b) obtain data on the oxidation response of these claddings via TGA (Thermogravimetric Analysis) techniques.
- (c) Microstructure and microchemistry of laser clad materials are determined using various electron optical techniques such as transmission electron microscopy, scanning electron microscopy and energy dispersive X-ray analysis. Special micro-diffraction techniques such as Convergent Beam Electron Diffraction (CBED) have also been used to identify the crystal structure of small submicron phases formed during laser cladding.
- (d) Differential Thermal Analysis (DTA) techniques were also applied to obtain information on the phase transformation temperatures of these metastable phases and finally this data was used to get an idea of the nonequilibrium phase diagrams in these systems.
- (e) Also the microchemistry and crystal structure details of the samples oxidized in the TGA were studied using Auger Electron Spectroscopy (AES) and X-ray photofluorescence Spectroscopy (XPS) to learn about the mechanism of oxide layer formation and the nature of adherence of the oxide scale to the substrate.

The scientific merit of the work is an improved understanding of the mechanism of metastable phase formation during rapid solidification and their effect on high

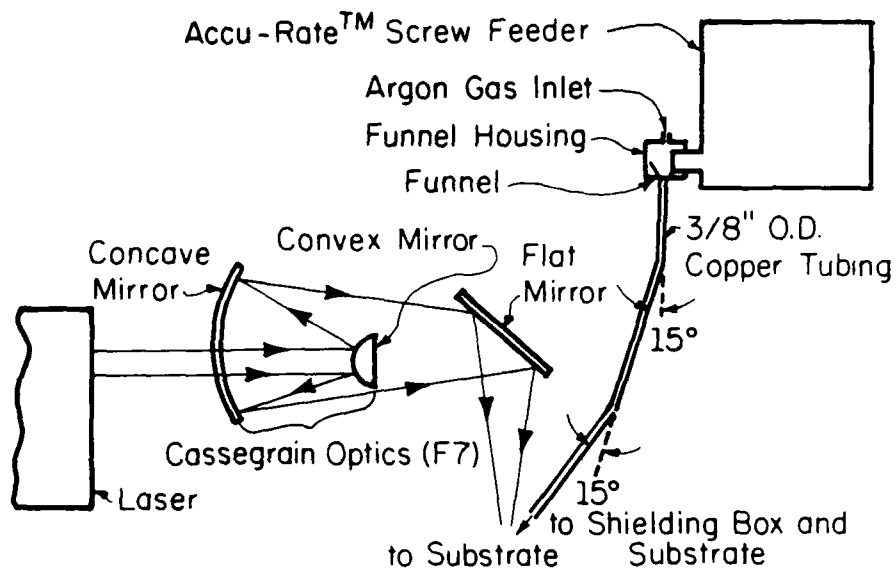


Fig. 1 Experimental setup for laser cladding.

temperature oxidation properties. This would in turn help us to produce a high temperature oxidation resistant material for both nickel and niobium alloys.

The details of the procedure used to perform the laser synthesis of Ni-Al-Cr-Hf on Rene 80 substrate, Nb-Al, Nb-Al-V, Nb-Zr on pure Nb and Zr on Mg are very much the same and they have been presented in previous reports or published papers [3,4,5]. However, the specific values of the process parameters varied with the alloy systems and the substrate material chosen. Process parameters for laser clad nickel based alloys are given in Table 1 below.

Table 1 Process parameters for Laser Cladding of Ni-Based Alloys

Material	Nominal Powder Composition at. %	Powder Feed Rate g/sec	Laser Power KW	Beam Dia. mm.	Traverse Speed mm/sec	Shielding Gas and Flow Rate gm/sec	Beam Position	Comments
Ni:Al:Cr:Hf	59:26:13:2 58:26:12:3	0.2	5 6 7	3	14.8 to 25.4	7.7 Argon	over- & under focussed	good clads
Ni:Al:Cr:Hf	70:20:7:3	2.2	5 7 9	3	19	Argon & Helium	under-focussed	good clads
Ni:Hf	90:10	1.7 to 2.7	6 & 4	3	21.2	Argon	under-focussed	good clads

The details of the microstructure evolution in the quaternary systems have been presented earlier in AFOSR reports [3,4]. However, the more important findings in the different systems are listed below.

2.1.2 Results and Discussion

(I) Ni:Cr:Al:Hf 59:26:13:2 and 58:26:12:3 (at.%) on Inconel 718, Iron and Rene 80 substrate

- (a) The clad structure with uniform distribution of undissolved hafnium, hafnium rich intermetallic precipitates and matrix with extended solid solution of Hf [4].
- (b) The oxidation response of the claddings produced by an underfocused beam geometry was better than that for an overfocused beam geometry [4].
- (c) The volume fraction and size of the γ' precipitates depend upon the laser processing conditions[4].
- (d) The γ' dissolution temperature was found to be $\sim 100^\circ\text{C}$ higher than the conventionally produced Ni-based superalloys used as the substrated material [4].

(II) Ni:Al:Cr:Hf 70:20:7:3 (at.%) on Rene 80 Substrate

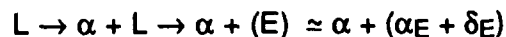
- (a) These claddings microstructurally consisted of γ' mostly in the form of dendrites, together with a small amount of eutectic constituents. There was also some amount of undissolved or partially dissolved Hf particles [3].
- (b) The eutectic structure was a mixture of two phases which are Hf rich (δ_E phase) and Hf lean (γ'_E phase) [3].
- (c) The δ_E phase is a heavily faulted f.c.c structure [3].
- (d) Microchemistry studies indicate that the extent of Hf in terminal solid solution (γ' phase) is about 13 wt% which indicates an order of magnitude extension in the solid solubility as compared to conventionally cast superalloy [3].
- (e) Laser processing parameters, e.g. laser power, traverse speed, etc., influences the morphology of the APBs in γ' phase.
- (f) The $\frac{1}{2} a_0 \langle 110 \rangle$ APB vector appears exclusively in this system in the γ' phase [3].

Overall, the oxidation resistance of the 70:20:7:3 claddings was superior to that for both the substrate and the 58:26:12:3 or 58:26:13:2 claddings based upon TGA and unoxidized metal thickness measurements. The surface scale of oxidized samples of the 70:20:7:3 claddings contained more Al and less Cr than those from the 58:26:12:3, 58:26:13:2 claddings and the substrate.

(iii) Ni-Hf Binary

Recently a paper entitled "Microstructure Evolution and Nonequilibrium Phase Diagram for Ni-Hf Binary Alloy produced by Laser Cladding" is published by Acta Metallurgica [6].

This paper mainly discusses the microstructure evolution and resultant metastable phase diagram for laser cladding of Ni-26 wt.% of Hf powder mixture on a pure nickel substrate. The microstructure of these alloys consist mainly of dendritic α -phase and a eutectic phase mixture. The α -phase is a f.c.c phase $a = 3.60 \text{ \AA}$ and the point group being $m\bar{3}m$ and the space group being $Fm\bar{3}m$. The hafnium content of the α -phase formed by this process is about 11 to 13 wt%, which is much higher than that which can be obtained by conventional processes. This also supports the theoretical prediction published earlier in Acta Metallurgica [7]. The eutectic phase mixture consists of δ_E (hafnium rich) phase and α_E (hafnium lean) phase. The δ_E phase is a nonequilibrium hereto unreported phase and has a tetragonal crystal structure with $a \approx 3.792 \text{ \AA}$ and $c \approx 5.264 \text{ \AA}$ and has a $4mm$ point group and $I4mm$ space group. The crystal structure and chemistry of α_E is essentially similar to the α phase. Due to the quick cooling process which is inherent of the laser cladding process the eutectic point is shifted to higher Hf concentration. On the basis of microstructural studies a possible phase transformation sequence (or microstructured evolution sequence) could be forwarded.



where the symbols L = liquid phase and E = Eutectic phase mixture. A nonequilibrium phase diagram is also presented for the Ni-rich end of the Ni-Hf system under laser cladding conditions.

2.2 Oxidation Properties

In this section, we will examine the effects of the laser cladding process on the oxidation resistance of Ni-based superalloys containing reactive elements such as Hf.

Investigation of the properties of laser clad Ni-based alloys containing reactive elements is aimed at improving the fundamental understanding of oxidation behavior of this class of alloys. As a rapid solidification process, laser cladding allows for significant extension of solid solubility and for the development of novel microstructures. The impact of these features upon the oxidation behavior of these alloys may help determine the nature of the beneficial effect produced with reactive element additions.

The laser cladding process offers certain advantages as a means of applying oxidation resistant alloys to components. Portions of components which require especially high oxidation resistance, such as the leading edge of a turbine engine blade, can be laser clad with the appropriate alloy while the remainder of the component can be of a composition dictated by other design criteria such as creep. This local application of the alloy may reduce the usage of certain strategic materials such as cobalt. Also, this process promises the fabrication of components with novel microstructure in near net shape by building up successive layers by laser cladding. If the oxidation resistance of the component can be significantly improved, higher operation temperatures that provide improved energy efficiency may be considered.

2.2.1 Experimental Procedure

Details of the background of the work undertaken are given in previous progress reports as well as a review of the relevant oxidation literature. This information is also given in two papers submitted for publication [8,9]. It is important to recall that several mechanisms have been proposed by various workers to explain the beneficial effect of reactive elements in Fe, Co and Ni alloys and the study of these mechanisms is still very active for both conventionally prepared and rapidly solidified specimens.

Since the last report, several authors have reported additional work on the adherence of alumina scales formed on Fe and Ni based alloys [11-14]. These authors concluded that sulfur segregation to the scale-metal interface during oxidation was responsible for the lack of alumina scale adherence and the addition of reactive elements, specifically Y, drastically reduces this segregation and consequently improved the scale adherence. No recent information regarding the effects of rapid solidification were included in these studies.

The techniques used for both laser cladding and the oxidation testing are discussed in the progress reports and the related manuscripts [8-10].

2.2.2 Results and Discussions

The 70Ni-20Al-7Cr-3Hf (atomic %) clads exhibited better oxidation resistance than the commercial Ni-based superalloy substrate, Rene 80, and the 58Ni-12Al-26Cr-4Hf clads. Figure 2 shows that the 70Ni-20Al-7Cr-3Hf samples, denoted as J, K, and L, gained less weight than the 58Ni-12Al-26Cr-4Hf samples, listed as 2RE1, 2RE3B, and 2RE5, and the substrate during testing at 1200°C in slowly flowing air for the eight hours of test. Table 2 indicates that less metal was lost on a thickness basis by samples of 70Ni-20Al-7Cr-3Hf than those of 58Ni-12Al-26Cr-4Hf and the substrate.

WEIGHT GAIN PER UNIT AREA AS A FUNCTION
OF TIME AT 1200 C IN SLOWLY FLOWING AIR

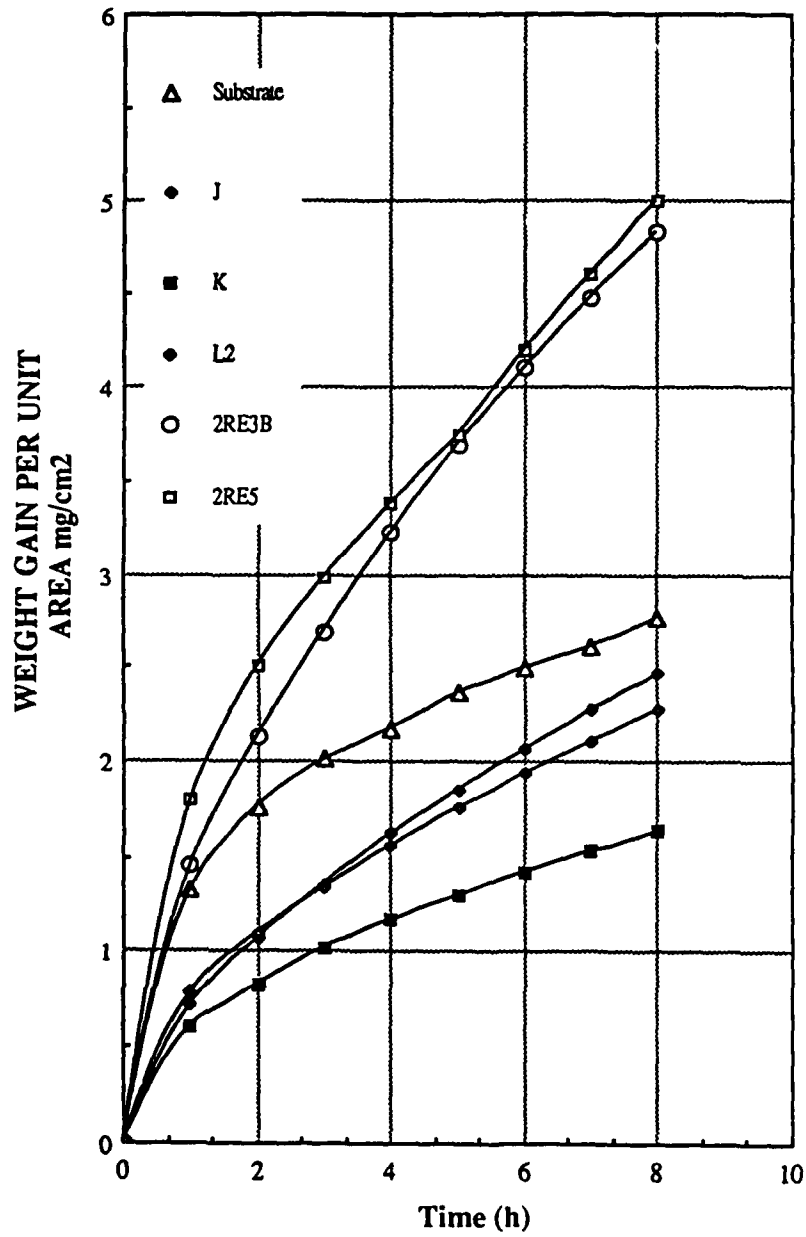


Fig. 2 Weight gain/unit area as a function of time at 1200°C in slowly flowing air.

Table 2 Comparison of Unoxidized Sample Thickness
with Original Sample Thickness

Sample	No. Measures	Original Thickness (mm)	Mean Unoxidized Thickness (mm)	Metal Loss (mm)
2RE1	4	0.18	0.14	0.04
2RE3B	4	0.22	0.18	0.04
2RE5	5	0.13	0.081	0.05
Substrate	5	0.21	0.12	0.09
K	3	0.36	0.33	0.03
L1	3	0.25	0.23	0.02

(Readings taken at 0.4 mm intervals except L1 where the interval used was 0.1 mm due to smaller sample dimensions.)

Microchemical analysis of the surfaces of the oxidized samples was performed using Auger electron spectroscopy (AES). Figure 3 is a typical plot of the derivative of the electron count as a function of the electron energy for the oxidized surface of a 70Ni-20Al-7Cr-3Hf sample. Heights of the characteristic peaks were divided by the appropriate sensitivity factors to allow calculation of the approximate composition of the surface as shown in Table 3. (Carbon was not included in the analysis since its presence was believed to result from contamination from either ambient conditions (prior to testing) or the spectrometer chamber itself; sputtering for up to 10 minutes reduced the carbon content but did measurably affect the amounts of the other elements detected.) Surface oxides of very high aluminum content were formed on the 70Ni-20Al-7Cr-3Hf samples while the 58Ni-12Al-26Cr-4Hf clads were covered with scales rich in Ni and Ti. Figure 4 indicates the uniform distribution of Al on the surface of an oxidized 70Ni-20Al-7Cr-3Hf specimen.

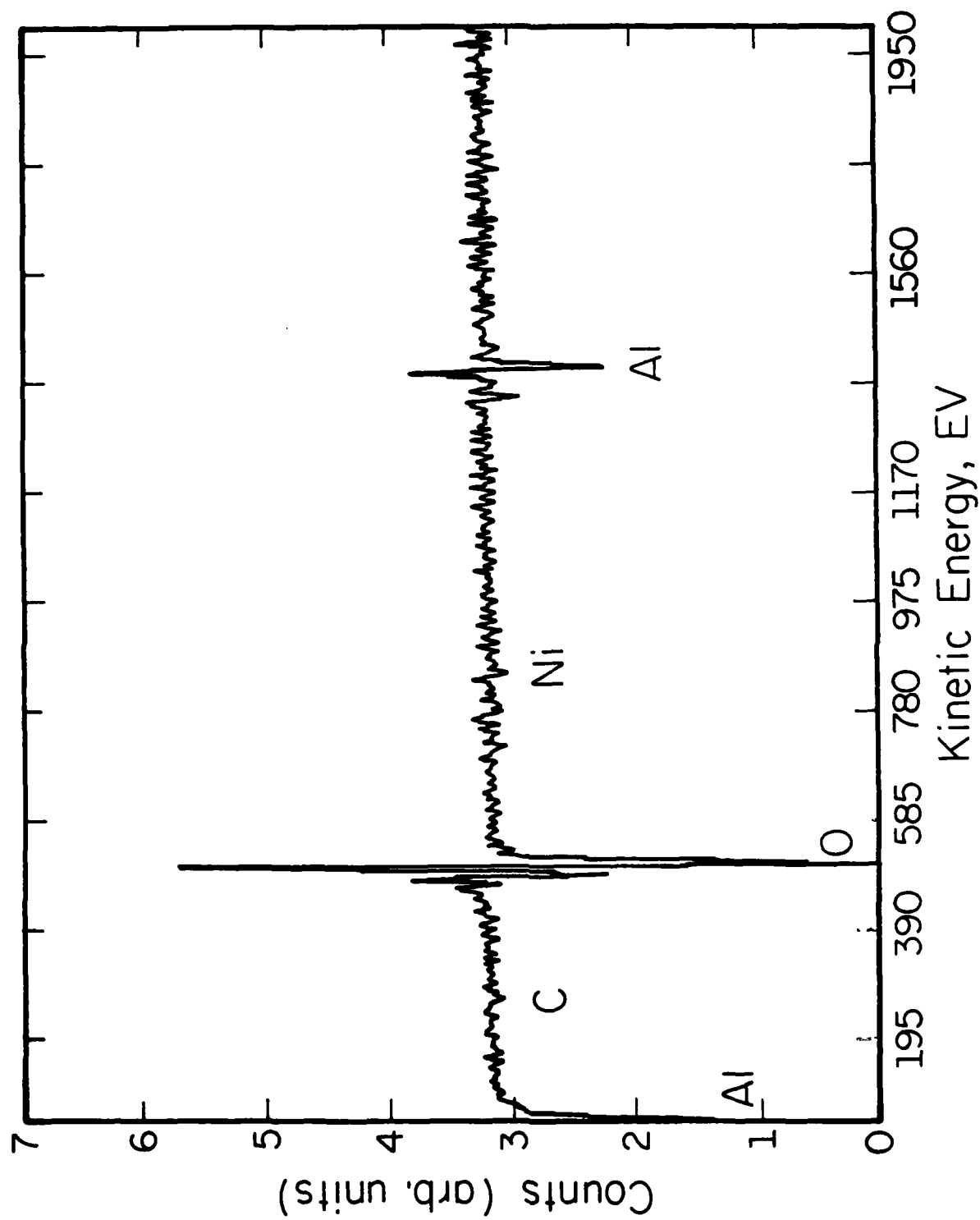


Fig. 3 Typical plot of the derivative of the electron count as a function of the electron energy for the oxidized surface of a 70Ni-20Al-7Cr-3Hf (at%) sample.

Table 3 Composition of Surfaces of Oxidized Samples
Using AES Excluding Carbon (Atomic %)

Sample	kV	Al	Cr	Ni	O	Ti
Substrate	5	—	—	17	54	29
J	5	50	—	3	37	—
K(A)	5	54	—	3	38	5
K(B)	5	56	—	5	36	3
L	3	68	—	4	28	—
2RE1(A)	5	14	10	29	32	15
2RE1(B)	5	—	16	40	40	4
2RE1(C)	5	22	—	6	57	15
2RE3B(A)	5	—	—	44	49	7
2RE3B(B)	5	—	—	35	51	14
CRE5	5	—	—	26	60	14

Examination of the cross-sections of oxidized samples of 70Ni-20Al-7Cr-3Hf clads revealed a number of Hf-rich oxide protrusions, encapsulated in aluminum oxide, penetrating into the unoxidized underlying alloy. Figure 5 is a secondary electron image of a typical cross-section along with the corresponding X-ray maps. AES analysis of regions within a large protrusion similar to that visible in Fig. 4 is given in Table 4.

Table 4 Approximate Composition of Regions of Large Oxide Protrusion
Similar to that in Figure 3 Based a AES (Atomic %)

Region	Al	Hf	W	Cr
Center	—	58	3	39
Outer Edge	55	17	5	23

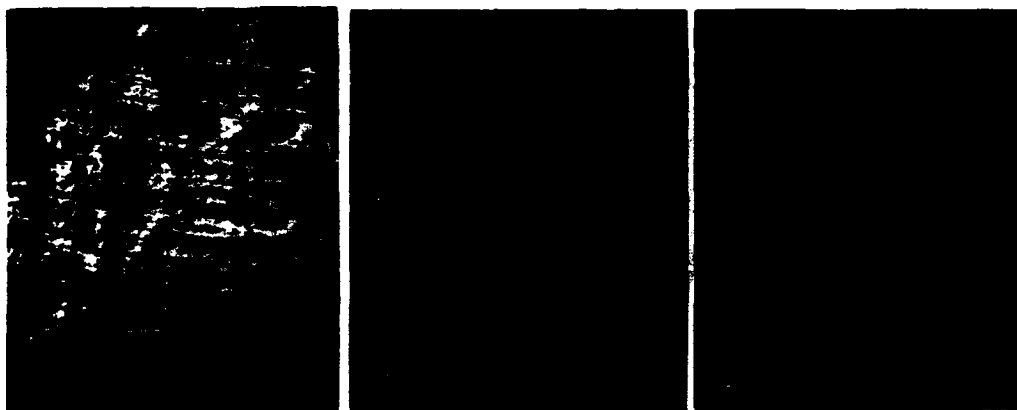


Fig. 4 Secondary electron image of oxidized cladding surface.
Auger electron elemental maps of (a) and (b) Al and (c) O.

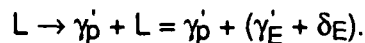


Fig. 5 Secondary electron image of a typical cross section in
70Ni-20Al-7Cr-3Hf (at%) along with the corresponding
X-ray maps.

The results indicate that 70Ni-20Al-7Cr-3Hf clads develop aluminum rich oxide layers during oxidation while both the substrate and the 58Ni-12Al-26Cr-4Hf alloy clads do not. The superior oxidation resistance of the 70Ni-20Al-7Cr-3Hf alloy is due in part to the relatively high aluminum content of the alloy.

2.3 Conclusions

The 70Ni-20Al-7Cr-3Hf laser clad alloys produced a 70% (approximately) γ' structure along with some eutectic structure and some undissolved Hf particles. There is about an order of magnitude increase in the Hf concentration, indicating solid solubility extension in the terminal γ'_p phase. The microstructure evolution may be explained as:



In the case of the 58Ni-12Al-26Cr-4Hf, the microstructure mainly consisted of undissolved hafnium rich intermetallic precipitates and matrix of $(\gamma + \gamma')$ with extended solid solution of Hf. The oxidation response of these clads are enumerated below:

1. The oxidation resistance of the 70Ni-20Al-7Cr-3Hf laser clad alloy is superior to that of both the 58Ni-12Al-26Cr-4Hf clad alloy and the substrate material, a commercial superalloy.
2. The oxidized surface of the 70Ni-20Al-7Cr-3Hf laser clad alloy is high in aluminum content while the 58Ni-12Al-26Cr-4Hf clad alloy produced surface oxides rich in Ni and Ti.
3. High concentrations of oxidized Hf were found in aluminum oxide coated spikes penetrating into the unoxidized metal matrix.

2.4 Future Work

- (1) The internal defect structure in the δ phase needs to be studied carefully to understand the phase transformation in the system.
- (2) Further work needs to be done on the process parameter dependence of APB's in order to obtain a clearer picture of the mode of their formation.
- (3) Composition optimization needs to be performed in order to determine the ideal composition for high oxidation resistance coupled with high γ' dissolution temperature.
- (4) Further compositional analysis using int to be performed in order to obtain a more accurate microchemistry.
- (5) Determine how the cladding microstructure affects oxidation behavior using SEM and energy dispersive X-ray analysis (EDX) and AEM techniques.
- (6) Using AES, SEM and EDX techniques, determine the effect of Hf upon the oxidation resistance of the claddings.
- (7) Determine the cause of the cladding cracks and the means of avoiding such cracks using metallurgical techniques.
- (8) Determine if the samples from the 70-7-3-20 claddings actually passivate during oxidation testing by isolating the PtO_2 volatilization effects.

3. LASER CLADDING OF Nb-BASED SYSTEM

3.1 Experimental Procedure

As mentioned before in this class of materials also our objective is to understand the mechanism of metastable phase formation and the high temperature oxidation response of these metastable phases. The procedural details for obtaining the cladding are exactly similar to that of the nickel based system. The process parameters used for laser cladding of Nb alloys are given in Table 5.

Table 5 Process parameters for Laser Cladding of Nb Based Alloys

Material	Nominal Powder Composition at %*	Powder Feed Rate g/sec	Laser Power kW	Beam Diameter mm	Traverse Speed mm/sec	Shielding Gas	Beam Position	Comments
Nb-Al	NbAl ₃ Nb ₃ Al		5 to 9	3	10 to 25	Helium	under-focussed	
Nb-Al-V	NbAl ₃ +5at%V NbAl ₃ +10at%V NbAl ₃ +15at%V	1.2 to 1.8 gm/sec	5 to 9	3	10 to 25	Helium	under-focussed	Some amount of key-holing
Nb-Zr	Nb-50-at%Zr		5 and 6	3	10 to 20	Helium	under-focussed	Good Clads
*Composition mentioned in the text-refers to nominal composition, not the actual clad composition								

3.2 Results and Discussion

Mechanical mixtures of powders with nominal composition as shown in Table 5 were used to produce cladding on a pure Nb substrate. The NbAl₃ (nominal) claddings were extremely brittle and the high rate of cooling associated with laser cladding produced intense cracking throughout the sample. With the addition of V to this system, however, this tendency to crack was much less. However, even addition of 15at%V did not solve the problem of material brittleness and cracking completely.

So far we have not been successful in quantifying the ductility in these materials, mainly because of the cracking problem. We are in the process of making miniature (crack free) tensile samples in order to achieve this goal.

Both the Nb_3Al and NbZr showed a considerably less tendency to crack under the same cooling rates applied before.

We have performed TGA (Thermogravimetric Analysis) tests of these samples at 1200°C in air as a function of time. These results are shown in the graph in Fig. 6.

As the graph (Fig. 6) indicates, the material which shows the most resistance to oxidation amongst this group is the nominal NbAl_3 . Small additions of vanadium produces a dramatic change in the oxidation response in the system, i.e. the oxidation resistance deteriorates with the addition of vanadium to nominal NbAl_3 . Addition of about 15at%V produces clads which have nearly the same oxidation property as that of pure Nb.

Hence although the addition of vanadium to nominal NbAl_3 is good in terms of improving the ductility of the material, it however has an adverse effect on the oxidation response of the system. The oxidation response of Nb_3Al and NbZr (50 at% Zr) has also been shown to be very poor. Our approach to solving this problem is two fold. (a) Try to improve the ductility of NbAl_3 without losing the oxidation property by addition of other ternary and quaternary alloying elements like boron, Cl, Hf, etc.

In order to understand the reason behind the type of behavior in Nb-Al-V system, we have performed X-ray photofluorescence spectroscopy (XPS) studies of the oxides formed on the cladding surfaces using a Perkin Elmer XPS machine, $\text{MgK}\alpha$ radiation was used as the incident X-ray source. O 1s, Nb 3d, Al 2p and V 2p photoelectron peaks have been studied in great detail.

The results obtained indicate the presence of a variety of oxides depending on the alloy composition of the clads. This can be tabulated as follows

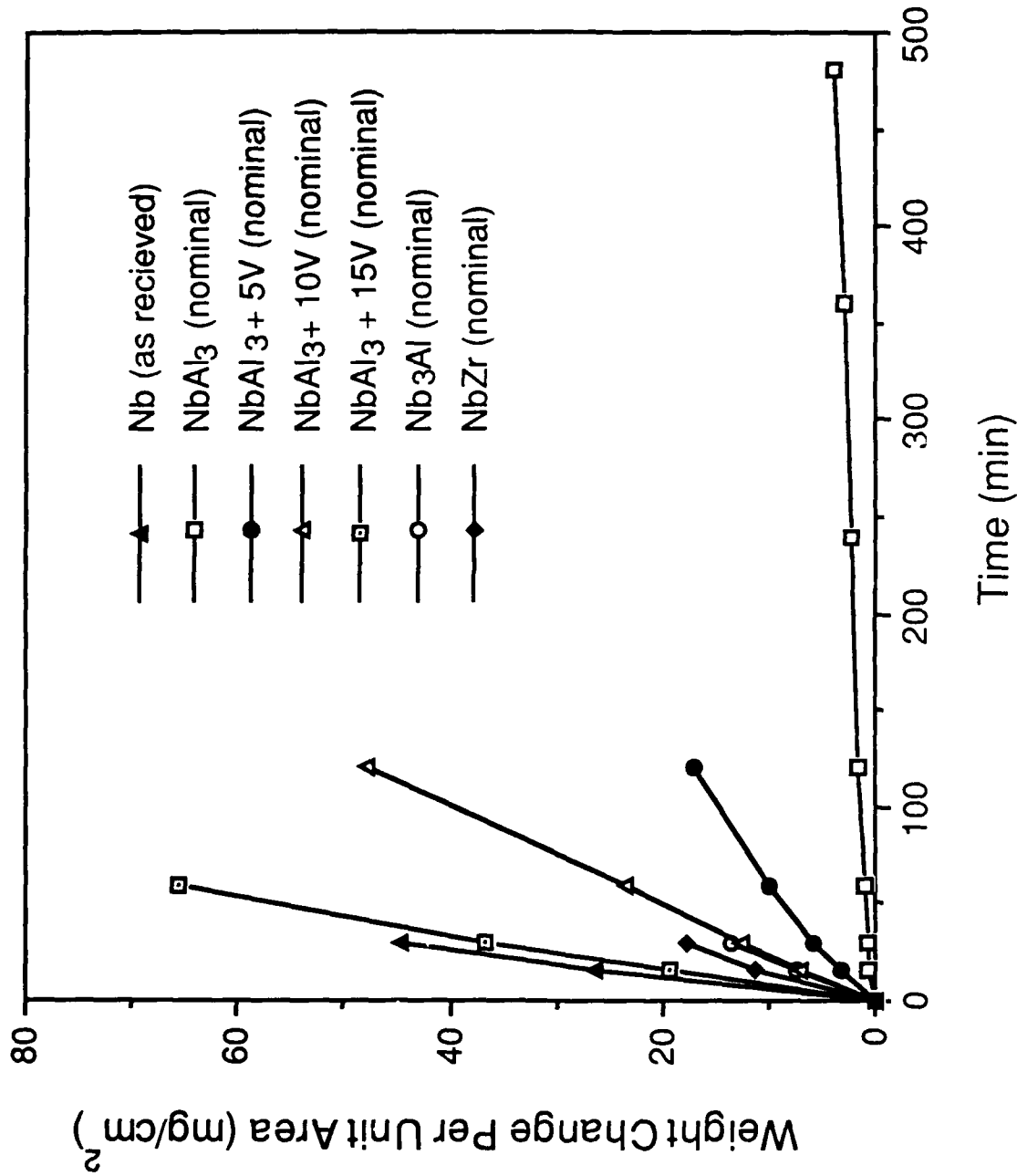


Fig. 6 Weight change/unit area for laser clad Nb alloys oxidized at 1200°C in air as a function of time.

Table 6 Oxides in Laser Clad NbAlloys after TGA

Alloy Compositions (nominal)	Oxides formed (1200°C in air)
Nb	Nb_2O_5
NbAl_3	$\text{Nb}_2\text{O}_5 + \text{Al}_2\text{O}_3 + \text{U O}$ (unknown oxide)
$\text{NbAl}_3 + 5\text{V}$	$\text{Nb}_2\text{O}_5 + \text{V}_2\text{O}_5 + \text{U O}$
$\text{NbAl}_3 + 10\text{V}$	$\text{Nb}_2\text{O}_5 + \text{V}_2\text{O}_5 + \text{U O}$
$\text{NbAl}_3 + 15\text{V}$	$\text{Nb}_2\text{O}_5 + \text{V}_2\text{O}_5 + \text{U O}$
Nb_3Al	$\text{Nb}_2\text{O}_5 + \text{U O}$

With addition of vanadium, the protective Al_2O_3 coating required for high temperature oxidation response is lost. Hence, addition of vanadium actually has an adverse effect on the oxidation response as indicated earlier. We are at present performing some X-ray diffraction studies of the oxides in order to determine the exact nature of the unknown oxide (believed to be complex Nb, Al, V oxide).

Optical microscopy studies conducted on these claddings indicate that both NbAl_3 and $\text{NbAl}_3 + 5\text{V}$ forms a dual phase microstructure which is composed of the dendrite and the interdendritic phase (Fig. 7). However, on addition of more vanadium (10 and 15 at.%) the microstructure is composed of at least three phases. Two of the phases are the dendritic structure and the interdendritic phase, described earlier, combined with a needle like martensitic phase. However, the exact nature of the third phase and its orientation relationship and habit plane, etc., needs to be determined via TEM procedures. The microchemistry and the extension of the solid solubility of V in the dendrites need also to be ascertained using EDX studies. However, it is quite obvious that the formation of the third phase in this system also has an adverse effect in terms of the oxidation response of the system.

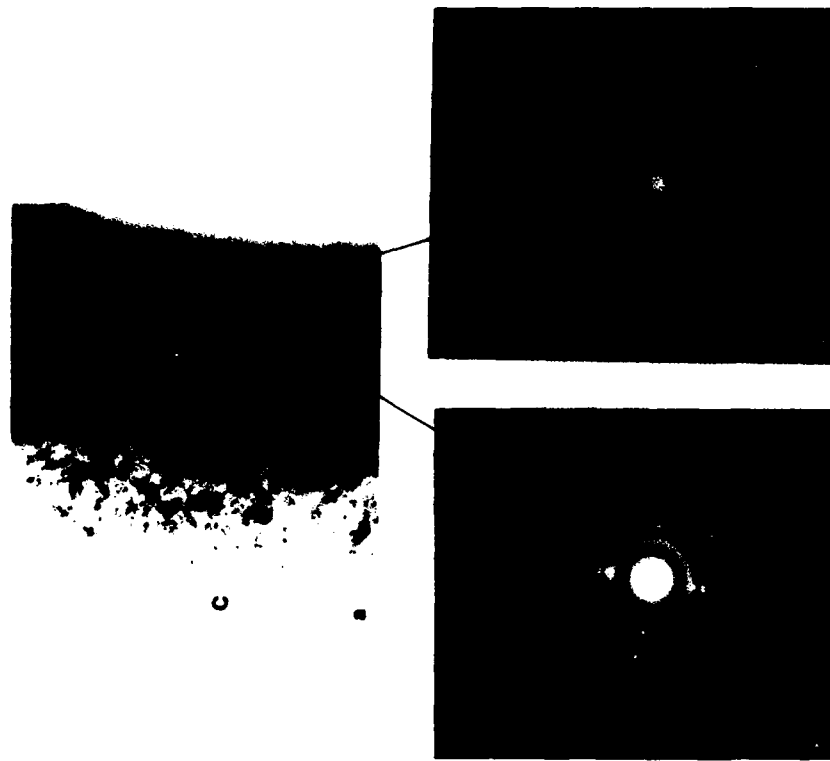


Fig. 8 (a) Electron micrograph of the laser clad region in Mg-Zr system (b) SAD pattern from amorphous phase and (c) SAD pattern from crystalline phase/amorphous interface region.

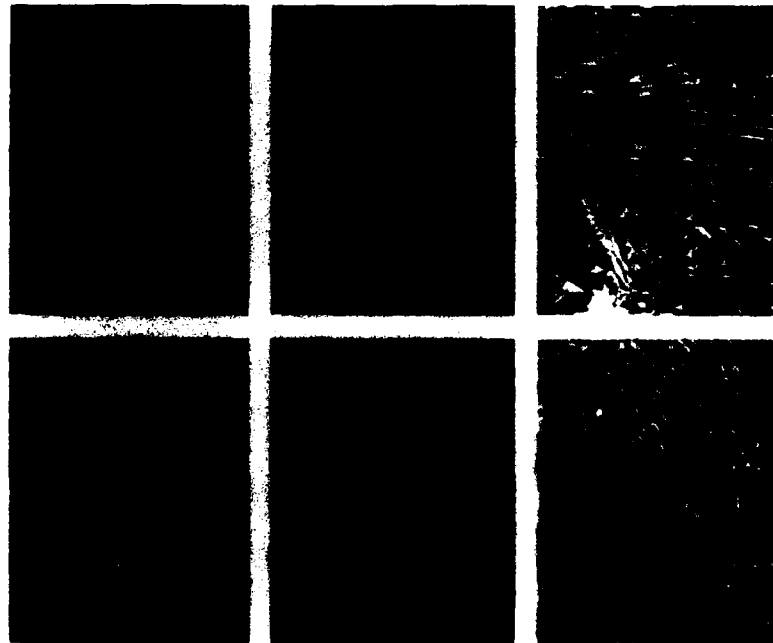


Fig. 7 Optical micrographs of various laser clad Nb-based alloys.

Both the Nb_3Al and the NbZr samples show a two phase dendritic structure as shown by the photomicrographs in Fig. 7.

Some similar work has also been done in the Nb-Ti system. The oxidation response of Nb-10wt%Ti, 20wt%Ti, and 30wt%Ti has been shown to be marginally better than pure Nb. The microstructural details (includes the formation of martensitic plates and an amorphous phase) have been presented elsewhere [3].

3.3 Conclusion

Laser cladding of nominal compositions of NbAl_3 , $\text{NbAl}_3 + 5$, 10, and 15 at% V, shows that the best oxidation response at 1200°C is shown by NbAl_3 (nominal). However, this is an extremely brittle alloy after, laser cladding. Addition of V help in improving the mechanical properties of the material, however it has a deleterious effect on the oxidation response in this system. Formation of martensitic phase in $\text{NbAl}_3 + 10$ and 15 at%V could be responsible for the change in the oxidation response of the material. Preliminary data on the Nb-10, 20, and 30 wt% Ti indicates that the oxidation response at 900°C is only marginally better than Nb. However, microstructure studies have indicated the presence of martensitic phases and also some amorphous phases in this system.

3.4 Future Work

At present, our most important obstacle is to impart ductility to the Niobium based alumides, specifically NbAl_3 . This has to be achieved without sacrificing the oxidation property of the NbAl_3 . We are in the process of producing clads with ternary additions to reach the above mentioned goal. Our experience with V additions is not positive. Although the ductility of NbAl_3 (nominal) improved due to V addition but the oxidation response is found to be extremely poor. The choice of ternary element addition would be based on various available theories on the oxidation of high temperature alloys, of

which the secondary gettering theory is perhaps very important. On the basis of this theory, which deals with the ΔG of oxide formation being intermediate between Al_2O_3 and Nb_2O_5 , the following elements may be chosen: Ti, Ta and Si. Hence our present approach is to utilize Ti as the secondary getter element and try to retain the NbAl_3 oxidation response (or improve on it) as well as improve the ductility.

It is also important to get some more basic information on the binary Nb-Ti, Nb-Al, Nb-Ta, Nb-Si systems in order for us to predict the properties of these materials in ternary or in quaternary systems.

At present we are also in the process of evaluating the crystal structure, phase separation and microstructure evolution process in the Nb-Al, and the Nb-Al-V system and try to obtain a basic understanding of the reason behind the change in the system properties with addition of vanadium.

4. CORROSION RESISTANCE PROPERTIES OF LASER CLAD Mg-Zr SYSTEM

4.1 Experimental Procedure

For the cladding of Zr on Mg, the dried zirconium powder was tightly packed in a shallow groove made on the magnesium substrate. Then the substrate with the powder was put inside a chamber and kept in an argon atmosphere at pressures above ambient. The laser beam (underfocussed, 1.5 to 3 mm dia. TEM₀₀ mode) was passed through a salt window and the cladding was achieved. Further details can be obtained from Ref. 5.

In the case of Mg-2wt% Zr and Mg-5wt% Zr, however, the in-situ laser cladding technique was adopted. In this case also, the chamber was pressurized by Argon gas to above ambient before cladding was done. Process parameters used in this study are listed as follows: The process parameters for laser cladding of Mg are given in Table 7.

Table 7 Process parameters for Laser Cladding of Mg Based Alloys

Material	Nominal Powder Composition at %*	Powder Feed Rate g/sec	Laser Power KW	Beam Diameter mm	Traverse Speed mm/sec	Shielding Gas and Flow Rates	Beam Position	Comments
	Pure Zr	Preplaced	1.5	1.5 to 3	8.4 to 21.1	not available	not-available	
Mg-Zr	Mg-2wt%Zr	0.355	3	5	16.35	Helium	under-focussed	Deep HAZ on the substrates. Needed double passes for hemispherical clads
	Mg-5wt%Zr	0.355	3	5	16.35	Helium	under-focussed	

4.2 Results and Discussion

(i) Cladding of Pure Zr on Pure Magnesium

a. Microstructure

General microstructural survey of the laser clad region using transmission electron microscopy revealed several phases: amorphous, crystalline and precipitate. Regions of martensitic platelike phases were also observed. Observation of the amorphous phase being a salient feature, is being discussed in detail here.

In a thin foil prepared from the clad region it was observed in the TEM that an amorphous region was adjacent to a crystalline region. This is shown in the bright field (BF) micrograph in Figure 8a. Figure 8b shows the selected area diffraction pattern (SAD) from the region marked 'A' in Figure 8a and the diffused rings shows that region 'A' is amorphous. Figure 8c shows the SAD pattern from regions marked 'B' and 'C' and consist of diffuse rings due to amorphous phase and diffraction spots due to crystalline phase in these regions.

X-ray microanalysis of the amorphous phase (region A) revealed that this phase contains 85.56 wt% Zr and 14.439 wt% Mg. X-ray microanalysis of the region B revealed that this region contains equal amount of Zr (50.56 wt%) and Mg (49.431 wt%). The X-ray microanalysis of the region marked C revealed that this region is rich in Mg (74.464 wt%) and depleted in Zr (25.536 wt%).

From the electron microscopic investigation in conjunction with X-ray microanalysis, an amorphous phase rich in Zr and an interface containing equal amount of Zr and Mg and an adjacent region rich in Mg were found. The amount of Mg increases as one move from the amorphous phase towards the interface.

Similar findings have also been observed in Cu-Zr system [15]. Amorphous surface layer 30 to 70 μm thick in the alloy Cu-43 at % Zr by laser radiation under suitable condition has been reported in the literature. It is reported that, even on

melting treatment at larger areas by overlapping pulse irradiation, the glassy structure may be retained in the topmost structure.

Capelli [16] has pointed out the attainment of amorphous alloys by laser glazing. The extremely rapid cooling rates of thin molten zones formed by laser interaction have produced a variety of novel, extremely homogeneous microstructure, including amorphous alloys.

b. Corrosion

The corrosion properties of the laser clad Zr on pure magnesium and that of magnesium have been evaluated. The results from corrosion potential tests and potentiodynamic test have been summarized and compared with other metal and alloy systems and shown in the Table 8 below.

Table 8 Corrosion Evaluation of Zr Laser Cladded onto Mg and Comparison with Other Alloy Systems

Corrosion Evaluation: Material:	3.5%-NaCl E-Corrosion
Zr-Laser Clad	-0.647
Al-Cold Rolled	-0.674
Al-Powder Compact	-0.733
Mg-Al Received	-1.335
Mg-As Received	-1.526
Mg-Alloy	-1.455

(ii) Cladding of Mg-2wt% and Mg-5wt% Zr on Mg

a. Microstructure

The study of the laser clad region in optical microscope shows that homogeneous microstructure was developed. Figure 9 shows the microstructure of the laser clad. In the microstructure, the substrate is identified as A and the clad region is identified as B. The interface is marked by the arrow. The good fusion between the clad and the



Fig. 9 Microstructure of the laser clad region in Mg-2wt%Zr and Mg-5wt% Zr system.



Fig. 10 Bright field electron micrographs of the laser claddings in Mg-Zr system, showing martensitic plates.

substrate can be seen. There are grains common to both the clad and the substrate. This is attributable to epitaxial regrowth of the melt pool on the underlying grain structure of the unmelted substrate.

Lath type martensitic plates of different sizes were observed during investigation by electron microscopy in the thin foil prepared from the Mg-5wt% Zr laser clad. Figures 10a and 10b show the bright field micrograph of the plates in different regions of the foil. The plates contain substantial dislocations. The composition of the plate shown Figure 10b was determined by EDAX. The EDAX spectrum from this plate is shown in Figure 11. The quantitative analysis of this spectrum shows that the composition of the plate is Mg-2.144 wt% Zr.

The crystal structure of the plate was determined by selected area diffraction. Figure 12 shows the bright field micrograph of an adjacent region of plates in the foil. Selected area diffraction patterns were recorded from the plate identified as A in Figure 12a. Figures 13a and 13b show the *selected area diffraction patterns* of the zones $[2\bar{1}\bar{1}0]$ and $[10\bar{1}1]$ respectively, obtained from this plate A. The c/a ratio of magnesium is 1.623. The c/a ratio calculated from these diffraction patterns is 1.626.

The compositions of these plates were determined using EDAX. The quantitative analysis of these spectra were carried out. The composition of the plate A was found to be Mg-2.711 wt% Zr. The composition of the plate B was found to be Mg-2.46 wt% Zr. The composition of the plate C was found to be Mg-2.46 wt% Zr. The equilibrium solid solubility of Zr in Mg is 3.6 wt% Zr. In the present work, in the case of Mg-5wt% Zr laser clad, it was found that Zr dissolves in Mg to an extent of 2.711 wt% under the process conditions given in Table 7. The compositions of these plates applies only to that portion of the clad/substrate interface present in the thinned foil.

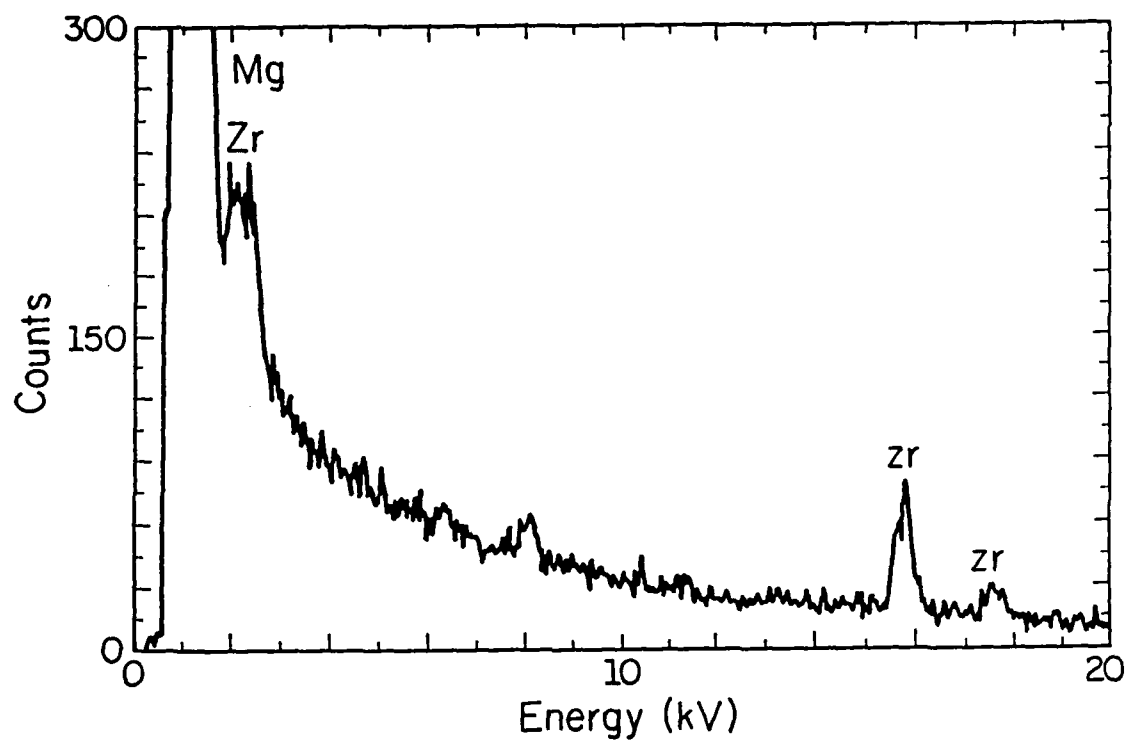


Fig. 11 EDAX spectrum obtained from the plate seen in Fig. 10(b).



Fig. 12 Bright field micrographs of the martensitic plate and the regions around it, in Mg-Zr systems.

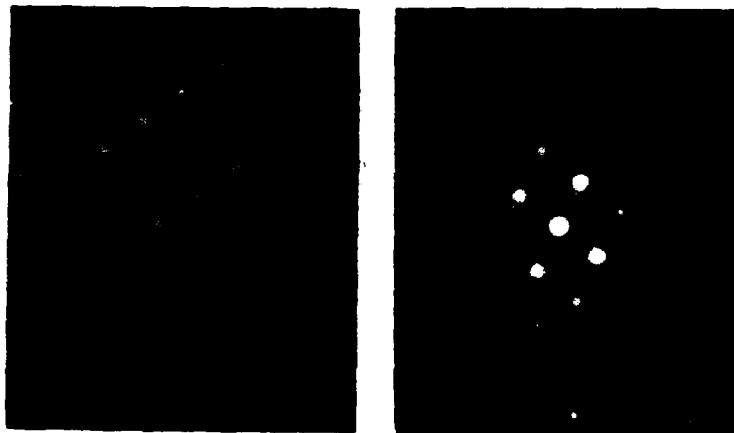


Fig. 13 (a) and (b) shows SAD patterns of zone axes $[2\bar{1}\bar{1}0]$ and $[10\bar{1}1]$ respectively from the plate A shown in Fig. 12.

b. Corrosion

Corrosion Testing

The corrosion behavior of the laser clad was evaluated by using EG&G PARC model 351 corrosion measurement system. This system consists of a model 1000 processor, a model 272 potentiostat, a corrosion cell and a plotter. The corrosion cell set up consists of a glass cell, specimen holder assembly, counter electrodes, bridge tube and saturated calomel electrode. A flat washer limits the area of the corrosion specimen to 1 cm² which will be exposed to the electrolyte. Two O-rings prevent leakage of electrolyte into the sample holder so as to eliminate crevice corrosion.

The corrosion specimens from the laser clad were prepared in the following manner. The top surface of the laser clad was ground to a flat surface on 600 grid emery paper. The low speed diamond saw was used to cut a sample of 0.003 m thickness from the laser clad as shown in Figure 14. From this sample, a disc of 0.015 m diameter was made by cutting with a low speed diamond saw and polishing on 600 grid emery paper to round the corners.

One corrosion cell set up is sufficient to carry out different corrosion tests using a fresh sample and fresh solution for each test. The corrosion cell set up for each test was made as described below. The specimen was immersed in the electrolyte, 3.5 wt % NaCl. The same solution was taken in the bridge tube which acts as the salt bridge. The narrow end of the bridge tube acts as a probe and was fitted with porous glass tip. The tip, 2 mm in diameter, is a semipermeable membrane. It provides ultralow liquid leakage rates and minimum IR drop through the tip. The bridge tube was positioned firmly in the corrosion cell using a clip and its position was adjusted to keep the distance between the tip and the surface of the corrosion specimen at 2 mm. The saturated calomel electrode was inserted into the open end of the bridge tube.

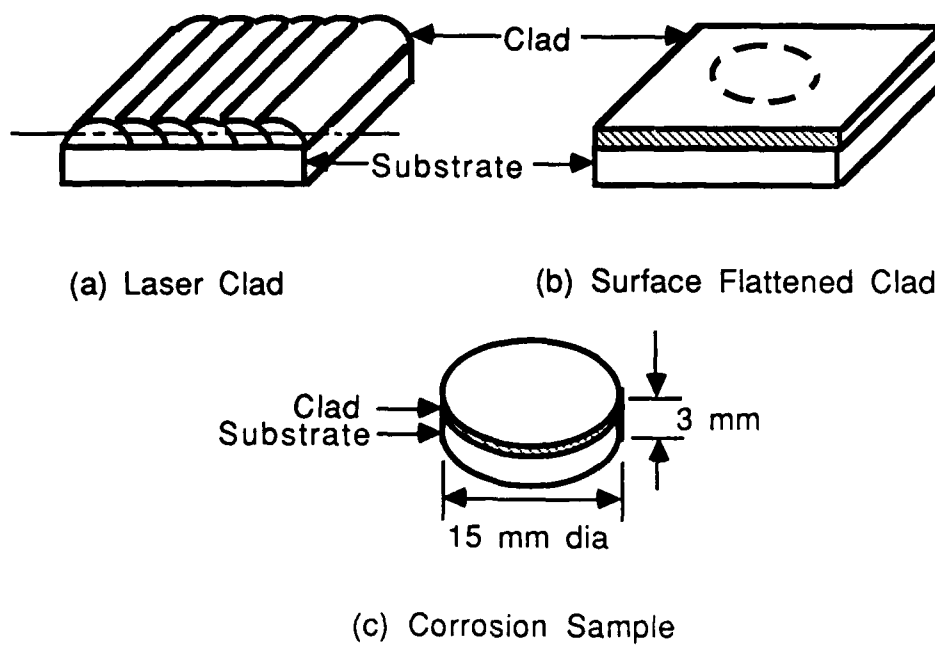


Fig. 14 Preparation of corrosion specimen from the clads.

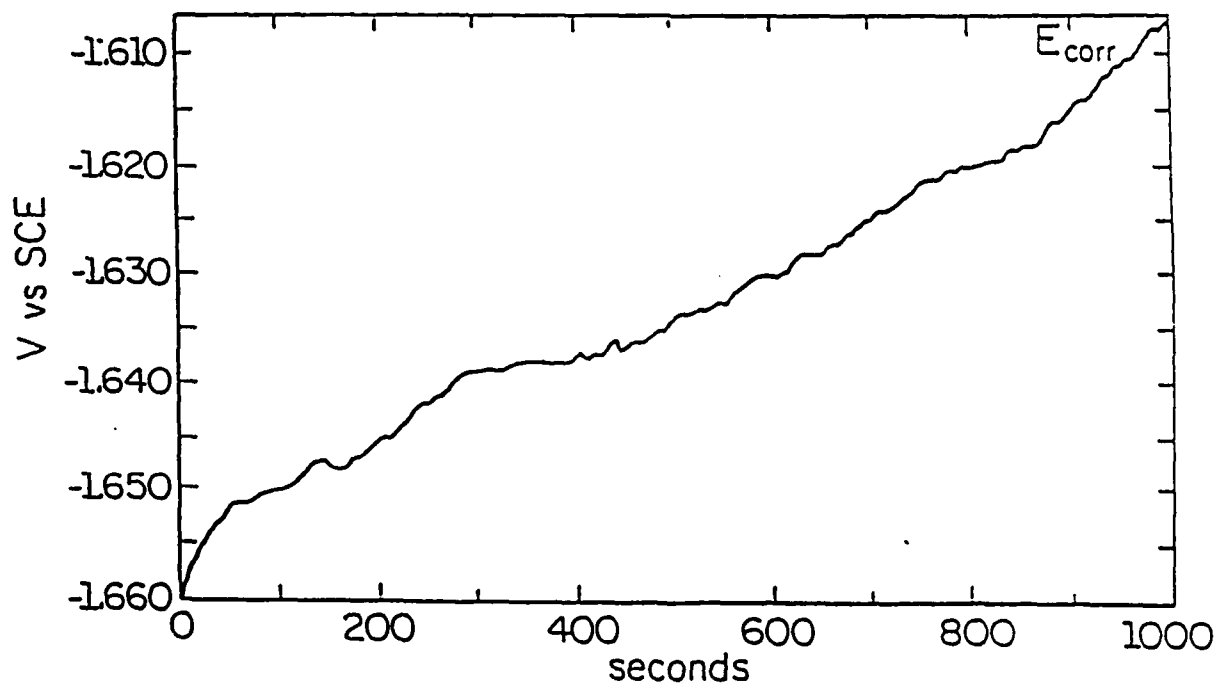


Fig. 15 Corrosion potential of Mg-2wt% Zr clad.

The experimental technique of each corrosion test is explained below. In all cases, the experiment was carried out by entering the test parameters in the model 1000 processor in conjunction with the model 272 potentiostat.

i. Corrosion potential (E_{corr}):

As soon as the corrosion specimen is immersed in the electrolyte, the test is initiated through the model 1000 processor. The potential at the surface of the specimen was measured with reference to the saturated calomel electrode as a function of time. The test was run for 1000 sec. and the equilibrium corrosion potential was read from the horizontal portion of the corrosion potential curve. From the corrosion potential measured, the position of the alloy in the galvanic series of metals in sea water can be determined. The corrosion potential of the alloys in the noble end of the galvanic series will be more positive than that of the alloys in the active end.

ii. Potentiodynamic anodic polarization test:

The corrosion specimen was immersed in the electrolyte. The initial delay was set to 1000 sec. As the potential was scanned from a value more negative relative to E_{corr} to a value more positive relative to E_{corr} , the current was measured and plotted as voltage versus logarithmic current density. The resulting plot is a potentiodynamic anodic polarization plot. From this plot, the current density at which the passive film forms can be found. The decrease in the current density as the potential is scanned in the anodic direction will indicate the change in the surface condition of the sample. Significant decrease in the current density is due to the formation of a protective film on the surface.

The corrosion potential of Mg-2wt% Zr laser clad was found to be -1.610 V versus SCE as shown in Figure 15. The corrosion potential of Mg-5wt%Zr laser clad has been found to be -1.57 V versus SCE as shown in Figure 16. The corrosion potential

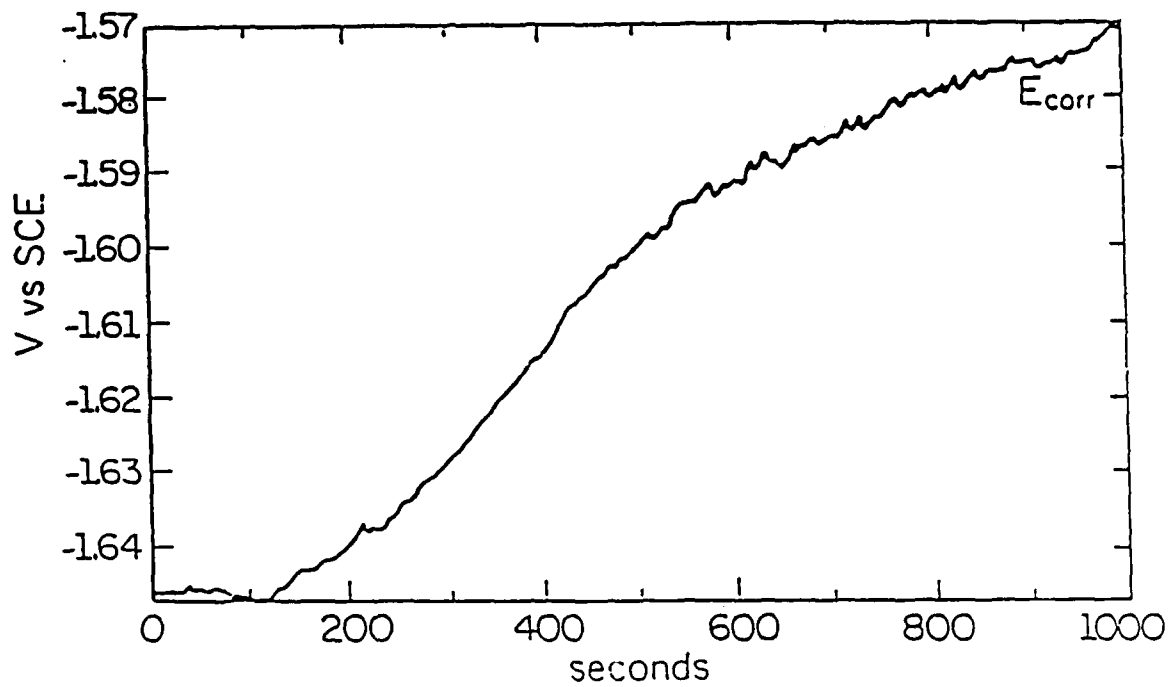


Fig. 16 Corrosion potential of Mg-5wt% Zr clad.

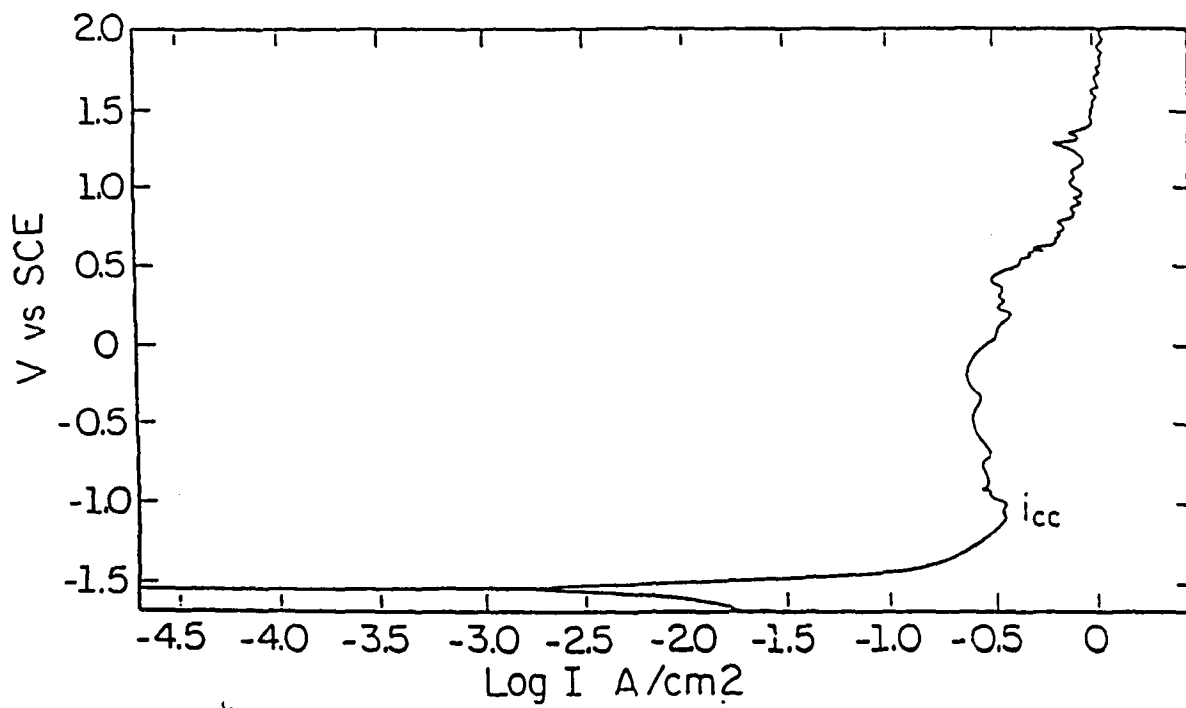


Fig. 17 Potentiodynamic anodic polarization test of Mg-2wt% Zr clad.

for 100% wt Zr on Mg is 0.647 V. The corrosion potential of magnesium in sea water is -1.66 V versus SCE. It seems that the corrosion potential of the laser claddings becomes more positive with increase in Zr addition. This shows that addition of Zr in Mg shifts the position of the laser clad towards the noble end of the galvanic series of metals in sea water.

The potentiodynamic anodic polarization plots of Mg-2wt%Zr and Mg-5wt%Zr laser claddings are shown in Figures 17 and 18, respectively. The incomplete passive film, in the case of both the laser claddings, forms at an anodic current density of 0.398 A/cm². Subsequent scan in the anodic direction results in the decrease of the current density to a minimum of 0.251 A/cm². Continued corrosion results in the pitting of the surface. This is in conjunction with the increase in the anodic current density as the potential is scanned further in the anodic direction.

The potentiodynamic anodic polarization plot of the alloy AZ91B is given in Figure 19. As seen from this plot, it is evident that there is no passive film formation in the case of alloy AZ91B. The anodic current density is 1.32 A/cm² which is much larger than that of the laser claddings. As the potential is scanned in the anodic direction, the current density stays constant at this value and rapid corrosion takes place. Addition of Zr to Mg seems to improve the resistance to corrosion in 3.5 NaCl solution.

4.3 Conclusions

The cladding of pure Mg with Zr gives rise to an improved corrosion resistant surface as compared to pure Mg. The production of an amorphous phase during the laser cladding process could have some effect on the corrosion property of the material. Further work needs to be done to understand this behavior.

The study of the laser clad region for the Mg-2wt% Zr and 5wt% Zr shows the development of a homogeneous microstructure. There are grains common to the clad

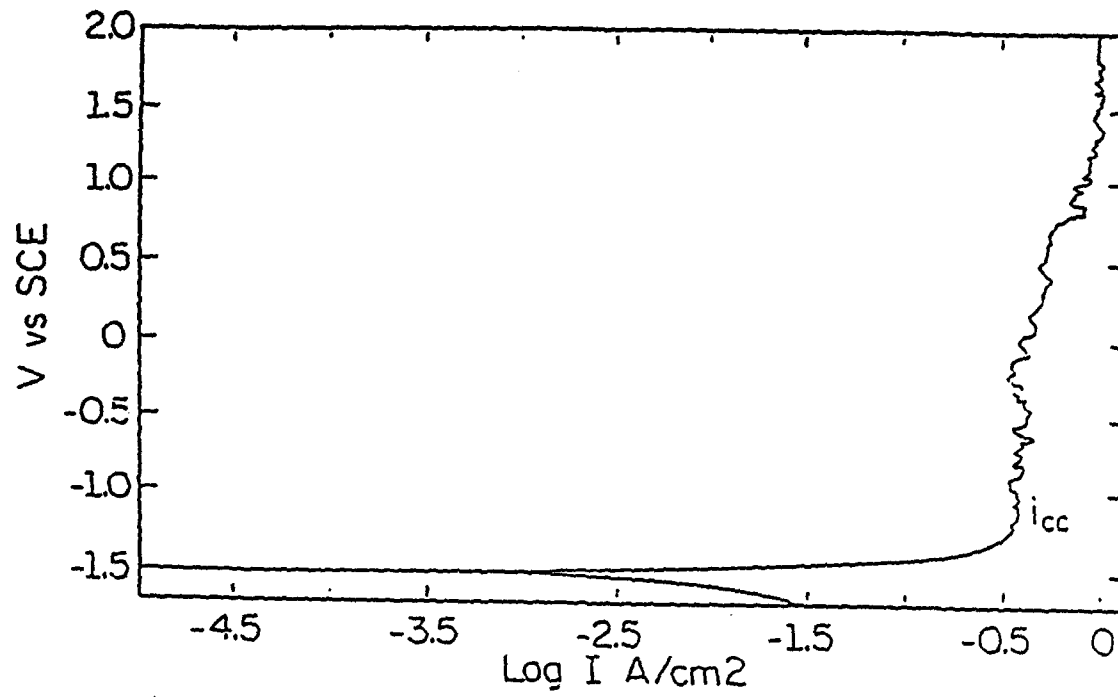


Fig. 18 Potentiodynamic anodic polarization test of Mg-5wt% Zr clad.

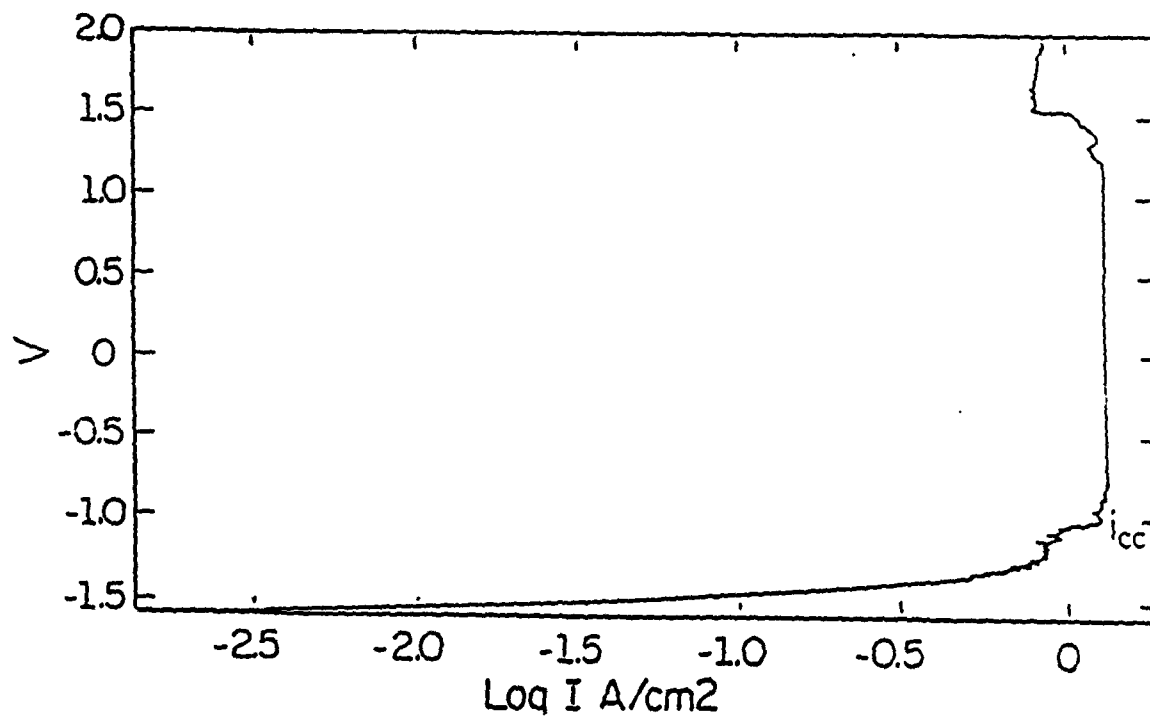


Fig. 19 Potentiodynamic anodic polarization test of Mg alloy, AZ91B.

region and the substrate. This could be attributed to the epitaxial regrowth of the melt pool on the microstructure of the unmelted substrate. Electron microscopy revealed mainly hcp martensitic structure for Mg-2 wt% Zr and Mg-5 wt% Zr alloys.

The addition of zirconium to magnesium shifts the alloy towards the noble side in the galvanic series of metals in sea water. Zirconium forms a passivating film on the surface which prevents further attack by chloride solution. The current density in the passivation region is reduced from 0.398 A/cm² to a minimum of 0.251 A/cm². It has been found that the laser cladding undergoes pitting type of corrosion in the NaCl solution. This is evident from the study of the surface of the corrosion sample of the laser clad subjected to the potentiodynamic anodic polarization test. The pitting on the surface was observed.

From the potentiodynamic anodic polarization test, it was found that the anodic current density in the passivation region of the laser clad is 0.298 A/cm² which is lower than that of the alloy AZ91B. Subsequent scan in the anodic direction results in the decrease in current density from 0.398 A/cm² to a minimum of 0.251 A/cm².

4.4 Future Work

Laser cladding of Magnesium has some inherent problems, which need to be addressed before a formal cladding process is employed. The single most important factor being the fact that Mg has a very high vapor pressure. Due to this property, claddings are liable to have a large amount of defects and porosities if conducted under atmospheric pressures. Preliminary work on magnesium system by Mazumder and Armendariz [29] indicated that the defects in the claddings can be greatly reduced by performing the cladding operations in an inert atmosphere and at pressures above ambient. With this idea in mind we have designed a chamber with X-Y stages and a built in powder delivery attachment. This unit operates well with the powder dispenser (screw feeder) discussed previously, and pressures as high as 5 p.s.i. above

atmospheric can be generated in the chamber. A salt window allows the laser beam in from the top surface of the chamber. The X and Y stages are moved using a Centroid controller.

This chamber is being utilized at present to produce claddings in various systems like: Mg-Al, Mg-Cl, Mg-Al-Cl, Mg-Cu. The reasons behind using these systems are many.

(1) In Mg-Al systems, addition of Al to Mg, has shown to improve the corrosion resistance of Mg [30] under rapidly solidified condition. However, the exact mechanism by which this is occurring is unclear. It is also reported the rare earth additions have a beneficial effect on the corrosion properties of Mg-Al alloys. We have chosen Ce to be the alloying element due to its comparatively lower melting points (in comparison to the other rare earths) and also since this cladding process involves low melting materials. In order to understand the effect of each of these elements we have undertaken a scheme wherein binary alloys will first be studied and the results obtained would be extended to ternary systems. This procedure, we believe, would help immensely in understanding the mechanism by which corrosion resistance is generated in this system.

The higher cooling rates achieved during laser cladding is extremely helpful in producing amorphous phases in various magnesium alloy systems. Magnesium is a very strong glass former with various binary and ternary alloying elements [31,41]. This glass forming ability of magnesium alloys is of vital importance as far as corrosion resistance is concerned [42].

Metallic glasses are free from defects associated with crystalline state such as grain boundaries, dislocations and stacking faults. Furthermore, rapid quenching from the molten state to prepare amorphous alloys prevents solid state diffusion during quenching. Thus they are also free from defects such as second phases, precipitates, and segregates, which are generally obtained during the process of slow cooling and

during heat treatment procedures. Amorphous alloys are, therefore, regarded as ideally chemically homogeneous alloys with respect to surface related characteristics such as corrosion. It is a well known fact that systems which show deep eutectics in the phase diagram are strong glass formers [33]. Based on this concept, the following systems may be singled out as prime candidates for amorphous phase formation. Mg-Ca [31], Mg-Cu [31,32], Mg-Ni [32], Mg-Pr [41], Mg-Zn [34-37], Mg-Nd [38,41], etc. At present, we have chosen Mg-Cu and Mg-Ni systems for performing the laser cladding process with an aim to achieving the amorphous phase as discussed earlier.

This study would also provide us with an indepth knowledge of microstructure-property relationship in the systems and answer some of the very fundamental questions in the area of corrosion protection of Mg-based alloys.

5. SPECTROSCOPIC STUDIES

5.1 Temperature Measurement

5.1.1 Experimental Procedure

The role of plasma during cw laser materials interaction is being studied using emission spectroscopy. The plasma is induced over a translating aluminum target in an argon atmosphere. The plasma diagnostic experimental set up is shown in Figure 20. The relative line to continuum method is used to calculate the electron number density and temperature values throughout each plasma. The attenuation and refraction of the laser beam as it propagates through the plasma column can then be calculated also [17]. The power was varied from 5 to 7 [kW] and the target translation speeds ranged from 0.4 to 2.5 [mm/s]. With an estimated error of $\pm 4\%$ the electron temperature distributions are presented through contour plots. The temperatures of the plasma cores are typically ranging as high as 20,000 [K] for our operating conditions. The plasmas generated in our experiments are commonly resemble a teardrop in shape, extending about 30 mm in length and about 8 mm in diameter.

5.1.2 Results and Discussion

In Fig. 21, isotherms at 13,000 [°K] depict the plasma outlines as the laser power is increased from 5 to 7 [kW]. As we would expect, higher incident laser powers will induce larger plasma volumes. We have also used the maximum plasma radii to gain insight into the behavior of the plasma volume as a function of both laser power and target translation speed. The maximum plasma radius data is plotted in Figure 22(b). The trends of Figure 22(b) clearly indicate that the plasma plume will increase as the laser power increases and also as the translation speed decreases. The increased interaction time at the lower translation speed aids the plasma formation process. The aluminum target samples were cross-sectioned and the width to depth

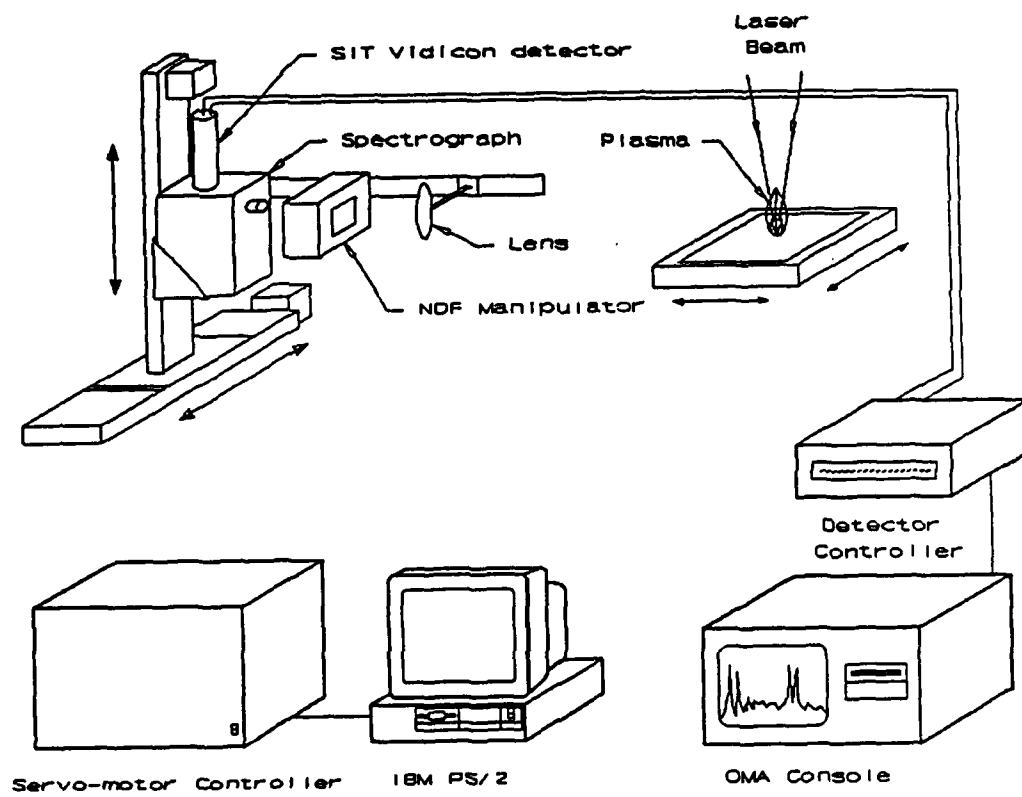


Fig. 20 Experimental setup of the emission spectroscopy system.

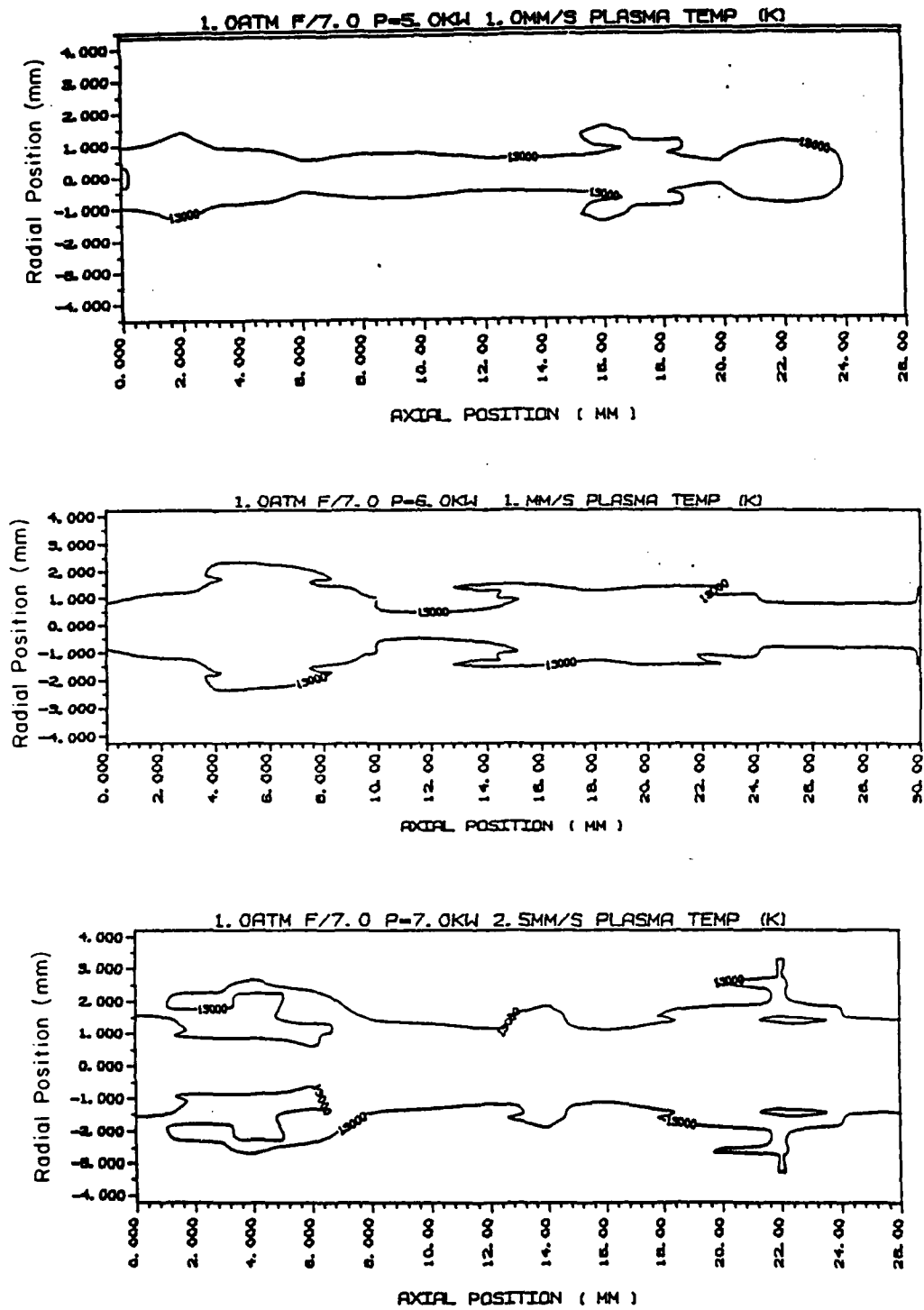


Fig. 21 Isotherms of 13000°K utilized in plasma volume characterization.

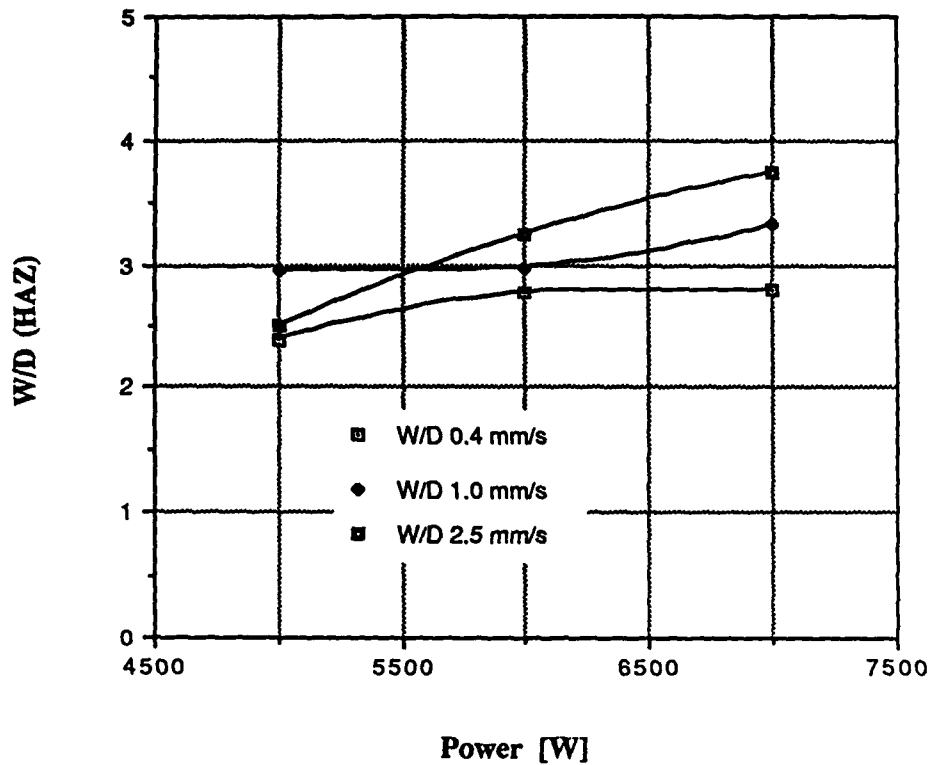
W/D ratio as a function of Power

Fig. 22 (a) Width to depth ratio of the HAZ as a function of laser power.

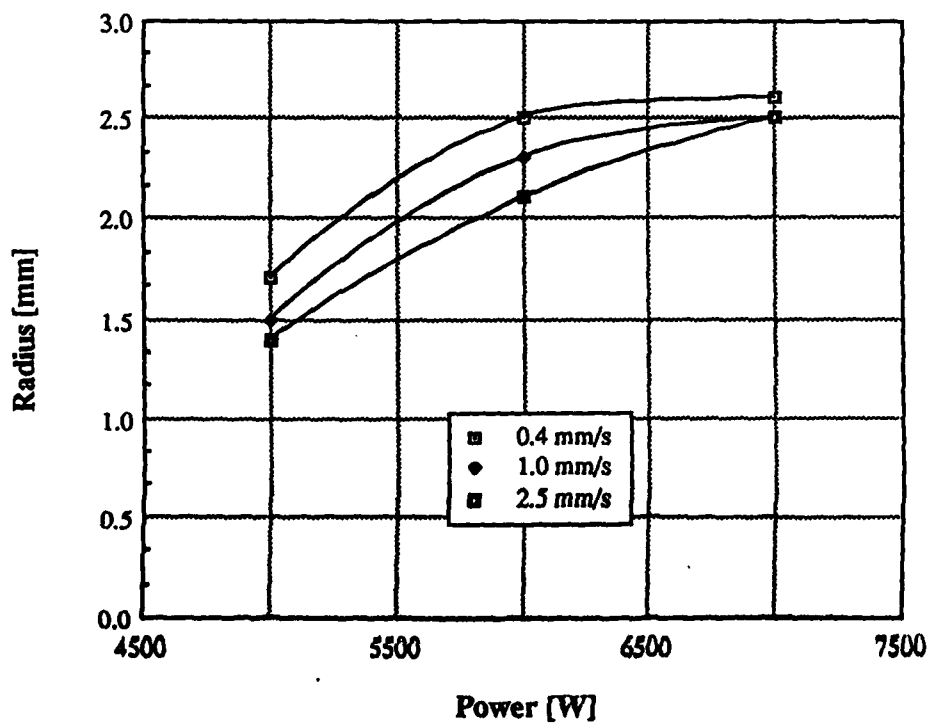
Maximum Plasma Radius

Fig. 22 (b) Maximum plasma radius as a function of laser power.

ratio of the heat affected zones (HAZ) is graphically presented in Fig. 22(a). The trends of Figure 22(a) indicate that the cross-section of the HAZ tends to flatten out (the width to depth ratio increases) as the translation speed of the target increases and also as the power increases. The width to depth ratio is on the order of 2 to 3, verifying that the energy transport mechanism at the surface of the target is conduction dominated with no keyholing occurring in any of the experiments. The width to depth ratio exhibits an almost linear relationship to the maximum plasma radius in Figure 23. The direct influence of the plasma volume on the shape of the HAZ demonstrates the manner in which the plasma refracts the laser beam as it propagates through the plasma. The absorption coefficients all fell in the range of 0.3 to 0.45 while the refracted laser beam radius ranged from 0.4 to 0.52 mm. These two properties tended to behave in a random method within their respective ranges, most likely because of a small air leak during the experiment which affected the assumption of a pure argon atmosphere made by the data reduction programs. A new experimental chamber has since been designed which will significantly increase the distance between the salt window and the location of the plasma, solving the air leak problem. Numerous other advances have also been made recently. Two-dimensional plasma intensity mappings have been acquired through spectroscopic data acquisition and are stored on an optical multichannel analyzer (OMA). The model 1460-V EG&G OMA has recently released a programmable operating system which allows BASIC programs to control virtually all the available utilities. Each plasma intensity mapping consists of numerous files, or "slices", which were individually recorded at equal increments along the axial direction of the plasma. Each of the files must be partially reduced using the OMA's utility functions before they can be transferred to the HP9000. Previously, each file was individually reduced and transferred by hand (numerically typed in) to the HP9000. A series of interactive BASIC subroutines has been completed which will reduce an entire set of files at once. For each file this

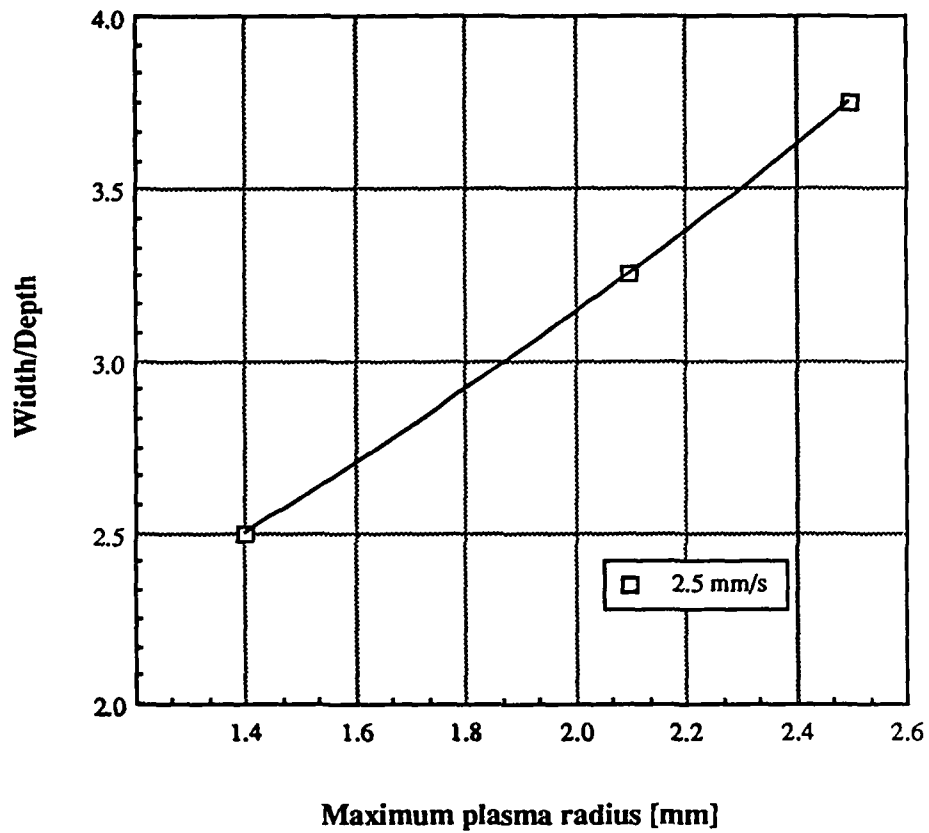
W/D ratio as a function of plasma radius

Fig. 23 Width to depth radius of the HAZ as a function of plasma radius.

entails subtracting the background intensity from the line intensity, integrating over the width of the plasma, and allowing the user to interactively select the centerline and endpoints of the file. Each file point is then converted from its 4 byte data storage form into ASCII strings and dumped into the HP9000 via an RS232 link. These advancements allow an order of magnitude increase in the speed of our data reduction process.

It is expected that after the spectroscopic technique for plasma diagnostics is developed, this will provide us with fundamental understanding of the role of plasma in laser surface modification processes.

5.2 Future Work: Concentration Measurement

Laser cladding of Mg alloys is a laser-induced plasma assisted processing technique generating a plasma of electrons and excited ions and neutral atoms during cladding. Measurement of the compositions in the liquid phase during cladding is important for process and control of composition during cladding. Conventional analytical technique such as spectrophotometry, X-ray fluorescence are unsuitable because they may be slow, require sample handling or be subject to interference by products and emitters in the solution to be analyzed [18].

Thus, there is a necessity for the development of an electro-optic based system to monitor in real time the composition and temperature of the cladding plasma and to quantify the composition of the plasma as a function of the compositions in the liquid phase. The emission spectroscopy of laser induced plasma has several advantages compared to the conventional methods. No sample preparation is required because only optical access is required to produce and observe the plasma. The technique is also fast. Such an analysis can reveal significant information concerning loss of alloying element due to vaporization [19] and hence clad composition during cladding.

This system is based on the fact that the intensity of light emitted by the plasma at wavelengths corresponding to the atomic transitions of an element is proportional to the element concentration in the plasma. By monitoring the emission from ionized species during claddings, it is possible to measure the concentration of the elements of interest in the plasma.

Equilibrium partial pressure of any species in the gas phase as a function of temperature is readily calculated [20] and hence changes in concentration of an element in the melt resulting in changes in the concentration of the element in the gas phase expressed in terms of partial pressure is evaluated. The melt pool compositional changes producing plasma compositional changes evaluated experimentally by emission spectroscopy and to quantify the spectroscopic results with the thermodynamical evaluation leading to the correlation of the composition of the plasma to the composition of the melt pool during cladding.

In order to determine the effect of the variations of the intensity of the plasma on vaporization flux, experiments conducted under different intensities of the plasma by changing the pressure in the reaction chamber. Also the experiments would unravel the dominant species in the melt pool and the dominant species in the plasma leading to the better understanding of the physics of the cladding process. Furthermore, the concentration profile of Magnesium and zirconium in the rapidly solidified laser clad pools obtained by secondary ion mass spectrometry and microanalytical techniques applied in understanding the structural and phase analysis of the laser clad material using TEM and SEM techniques.

The results obtained will give insight into the clad pool compositional changes during cladding by evaluating the compositions of its plasma and thus to monitor in real-time the composition of the clad during the process itself.

6. MATHEMATICAL MODELING OF EXTENDED SOLID SOLUTION IN LASER CLADDING

6.1 Current Work

We have developed a few mathematical models to understand the basics of laser cladding processes and to study the effects of various process parameters such as the laser power cladding powder feed rate, relative speed between the substrate and the laser beam, on the composition of the cladding. these models can also predict the extension of solid solubility that occurs due to rapid cooling in laser cladding. so far, we have modeled the laser cladding process by two different ways (1) by considering one-dimensional diffusion of heat and mass in semi-infinite mediums and (2) by considering one-dimensional diffusion of heat and mass in mediums of finite thickness. Besides this, we have also obtained expressions for nonequilibrium partition coefficients for concentrated and dilute solutions. These models have been developed for laser cladding processes as described below.

In laser cladding process the substrate material which is to be clad is moved at a constant rate while the cladding powder is poured onto it using a pneumatic powder delivery system and melted simultaneously by a laser beam. the uniform speed of the substrate and the constant feedrate of the cladding powder ensure uniform cladding thickness. the molten pool of the cladding material which forms just below the laser beam solidifies by dissipating heat to the surrounding air, adjacent cladding, and the solid substrate as it moves away from the laser beam. The shape of the cladding melt pool and the solidified cladding on the substrate is influenced by laser power, laser beam diameter, thermo-physical properties of the cladding powder and the substrate, temperature of the substrate, relative motion between the cladding powder delivery system and the substrate, the cladding powder feed rate and the interaction time between the cladding and the laser beam. The melt pool of the liquid cladding solidifies by conducting away heat through the substrate and the solid cladding. Also,

it loses some energy to the ambient inert gas across the free surface of the melt pool. However, the energy loss from the cladding melt due to conduction through the substrate and the solid cladding is much higher than that through the free surface of the melt pool.

(i) One-dimensional Infinite Medium Diffusion Model [21]

In this model, three one-dimensional transient heat conduction equations are solved to study heat transfer in the substrate, solidified cladding, and the liquid cladding. The thermal analysis allows us to determine the solidification rate that is the speed of the solid-liquid interface. Using this result, the one-dimensional mass diffusion equation is solved in order to determine the solute distribution in the melt pool. The concentration of solute in the solid phase, that is the extended solid solubility, is obtained by using an expression [22] for nonequilibrium partition coefficient. this model is based on the following assumption:

1. The thermal conductivity and the thermal diffusivity for a mixture is the sum of the volume averaged value of the respective transport properties of each element of the mixture.
2. The mass diffusivity of each element in the liquid phase is the average value of self-diffusivity over the room temperature and the initial temperature with modified activation energy for the mixture.
3. There is no diffusion of mass in the solid phase.
4. The solute segregated at the solid-liquid interface moves in the liquid phase by diffusion only.
5. The concentration of solute in the liquid alloy is equal to the nominal composition of the cladding powder mixture.
6. Change in solute concentration in the liquid phase does not alter its freezing point but it affects the heat flux across the solid-liquid interface.

7. only 50 percent of the laser energy has been assumed to be absorbed by the cladding material. Studies [23] show that the amount of laser energy absorbed by different materials is 37% to 60%.

Using this model, the change of cooling rate with time; variation of solute concentration with powder delivery rate, cooling rate, and cladding thickness are studied. Details of the model are available in Ref. [21].

(ii) One-dimensional finite-medium diffusion model [7,25]

In this model, the substrate and the cladding melt are considered to have finite thickness. In the previous model, the coupling between the heat and mass transfer equations is such that the heat equations can be solved first and then the mass transfer equations. This is not the case for this model because the sixth assumption of the previous model has been relaxed. The freezing point is considered to depend on the concentration of solute as given in Ref. [24]. Due to strong coupling between the heat and mass transfer equations, these equations have been solved by the method of Fourier transforms for multiregion problems. This model is based on the following assumptions:

1. The thermal conductivity and the thermal diffusivity for a mixture is the sum of the volume-averaged value of the respective transport properties of each element of the mixture,
2. The mass diffusivity of each element in the liquid phase is the average value of self-diffusivity over the room temperature and the initial temperature with modified activation energy for the mixture,
3. There is no diffusion of mass in the solid phase,
4. The solute segregated at the solid-liquid interface moves in the liquid phase by diffusion only,

5. The concentration of solute in the liquid alloy is equal to the nominal composition of the cladding powder mixture,
6. Change in solute concentration in the liquid phase does not alter its freezing point but it affects the heat flux across the solid-liquid interface,
7. Only 50 percent of the laser energy has been assumed to be absorbed by the cladding material. Studies [23] show that the amount of laser energy absorbed by different materials is 37% to 60%.

This model has been applied to study the extension of solid solubility in laser cladding of Ni substrate with cladding powder of Ni-Hf and Ni-Al systems. The composition of Ni in both cases was 74% by weight. The reason for studying these two systems is that the equilibrium phase diagrams of Ni-Hf and Ni-Al systems have negative and positive slopes, respectively, at the above composition. Thus, by studying these two systems we are able to investigate the effects of the signs of the slopes of the equilibrium phase diagrams on the extension of solid solubility due to rapid cooling in laser cladding.

For both systems, the effects of various process parameters such as the laser power, cladding powder feed rate, initial pool mean temperature, cladding thickness, etc., on the concentration of solute in the solid phase have been studied. Also, the nonequilibrium phase diagrams have been obtained for both Ni-Hf and Ni-Al systems. The extension of solid solubility predicted by this model has been found to agree well with experimental results.

(iii) Model for nonequilibrium partition coefficients [26]

In the previous two models, an expression [22] for nonequilibrium partition coefficient is used in order to determine the concentration of solute in the solid phase. The expression of Ref. [22] is actually applicable for dilute solutions. So, such an expression may be good for studying the rapid solidification phenomena of

semiconductor materials. In laser cladding processes, concentrated solutions are encountered quite frequently. In Ref. [27], one can find an expression for nonequilibrium partition coefficient for concentrated solutions. However, this expression has too many unknown parameters. In order to reduce the number of unknown parameters in the expression for nonequilibrium partition coefficient for concentrated solutions, we obtain the following expression by using the method of Ref. [28].

$$k = \frac{k_e}{k_e + (1 - k_e) e^{-(\bar{\beta} - \bar{\delta})}}$$

$$\bar{\beta} = \beta_c e^{-\alpha_A \rho m_I^* k_e}$$

$$\bar{\delta} = \sum_{n=1}^{\infty} \frac{\{\alpha_A \rho m_I^* (1 - k_e)\}^n - \{\alpha_A \rho m_I (1 - k)\}^n}{n \cdot n!}$$

$$\beta_c = ud/D_i$$

The diffusion coefficient of A in B is given by

$$D_{AB} = D_A(T) e^{\alpha_A \rho A}$$

where

k = nonequilibrium partition coefficient,

k_e = equilibrium partition coefficient,

ρA = concentration of A,

- ρ = density of the alloy
 m_i^* = mass fraction of solute at the solid-liquid interface in the liquid phase under equilibrium condition,
 m_i = mass fraction of solute at the solid-liquid interface in the liquid phase under nonequilibrium condition,
 u = speed of the solid-liquid interface,
 d = length of the diffusion zone,
 D_i = $D_A(T)$
 $\ln\{D_A(T)\}$ = intercept of the $\ln D_{AB}$ versus p_A graph,
 α_A = slope of the $\ln D_{AB}$ versus p_A graph

6.2 Future Work

The mathematical models that we have developed so far are one-dimensional and applicable to binary systems. These models utilize an expression of non-equilibrium partition coefficient which is not accurate for concentrated solution systems. Our plan is to eliminate these restrictions from our models and towards these objectives, we intend to do the following:

- (1) Examine non-equilibrium partition coefficient for concentrated solution.
- (2) Develop two- and three-dimensional models for laser cladding processes.
- (3) Use these models to predict the extension of solid solubility found in laser claddings and generate non-equilibrium phase diagrams.
- (4) Extend the binary system models to multi-component alloy systems.
- (5) Also, we want to study the formation of ripples in laser-melt liquid metal pools and its effect on the shape of the resulting solid formed from this melt pool.

REFERENCES

1. E. A. Aitken, Intermetallic Compounds, J. H. Westbrook, ed., pp. 503-506, John Wiley and Sons, New York, 1967.
2. R. C. Svedburg, Properties of High Temperature Alloys with Emphasis on Environmental Effects, Z. A. Foroulis and F. S. Pettit, ed.; pp. 331-362.
3. J. Mazumder, A. Kar, S. Sircar, C. Ribaudo, and R. Subramanian, "Laser Cladding of Ni, Nb and Mg Alloys for Improved Environmental Resistance at High Temperatures," Annual Report, Contract AFOSR 85-0333, 1987.
4. J. Mazumder, A. Kar, and J. Singh, "Laser Cladding of Ni + Cr + Al + Rare Earth Alloys for Improved Oxidation and Hot Corrosion, Annual Report, Contract No. 85-0333, 1986.
5. J. Mazumder, J. Singh, and S. Raja, Annual Report Contract #AFOSR 86-0034, Air Force Office of Scientific Research, 1987.
6. S. Sircar, J. Singh, and J. Mazumder, "Microstructure Evolution and Nonequilibrium Phase Diagram for Ni-Hf Binary Alloy Produced by Laser Cladding," Acta Metall. Vol. 37, No. 4, pp. 1167-1176, 1989.
7. A. Kar and J. Mazumder, Acta Metall. Vol. 36, 701 (1988).
8. Sircar, S., C. Ribaudo, and J. Mazumder, Proceedings of 1988 ESD/SPIE Symposium on Optical Engineering and Industrial Sensing for Advanced Manufacturing Technologies (to be published).
9. Ribaudo, C., S. Sircar, and J. Mazumder, submitted for publication in Metallurgical Transactions.
10. Singh, J., K. Nagarathnam and J. Mazumder, High Temperatures Technology, Vol. 5, No. 3, pp. 131-137 (1987).
11. Natesan, K., Oxidation of Metals, Vol. 30, No. 1/2, pp. 53-83, 1988.
12. Ramanarayanan, T. A., R. Ayer, R. Petkovic-Luton, and C. P. Leta, Oxidation of Metals, Vol. 29 No. 5/6, pp. 445-472, 1988.
13. Smeggil, J., and G. G. Peterson, Oxidation of Metals, Vol. 29, No. 1/2, pp. 103-118, 1988.
14. Sigler, D. R., Oxidation of Metals, Vol. 29 No. 1/2, pp. 23-43, 1988.
15. I. Pfeiffer and S. Hack, Z. Metallkunde, Vol. 72, No. 1, pp. 36-42, 1981.

16. P. G. Capelli, "Laser Surface Alloying," AGARD, Naho, (LS-106), pp. 13, March 1980.
17. T. Rockstroh, and J. Mazumder, J. Appl. Physics, Vol. 61, No. 3, pp. 914-923, 1987.
18. "Analysis of Uranium Solutions using Laser-induced Breakdown Spectroscopy," D. A. Cremers et al., p. 28, Topical meeting on Laser in Materials Diagnostics, Feb. 11-12, 1987.
19. "Spectroscopic Measurement of Hydrogen Contamination in Weld Arc Plasma," J. E. Shea, et al.: J. App Phys., Vol. 54, No. 9, Sept. 1983.
20. "Selective Evaporation of Metals from Weld Pools," T. W. Eager et al. Copyright 1982, A&M, Metals park, Ohio 44073.
21. A. Kar and J. Mazumder, J. Appl. Phys, Vol. 61, p. 2645 (1987).
22. M. J. Aziz, J. Appl. Phys., Vol. 53, p. 1158 (1982).
23. L. J. Li and J. Mazumder in Proceedings of Laser Processing of Materias, edited by K. Mukherjee and J. Mazumder (Metallurgical Society of AIME, Warrendale, PA, 1985, pp. 35-50).
24. W. J. Boettinger and J. H. Perepezko, Proc. Rapidly Solidified Crystalline Alloys, TMS-AIME, N.J. 1985.
25. A. Kar and J. Mazumder, Met. Trans. A., submitted.
26. A. Kar and J. Mazumder, Phys. Rev. B., submitted.
27. M. J. Aziz, Appl. Phys. Lett., Vol. 43, p. 552 (1983).
28. J. A. Burton, R. C. Prim, and W. P. Slichter, J. Chem. Phys. Vol. 21, p. 1987 (1953).
29. J. Mazumder and N. Armendariz, "Laser Cladding of Zr on Mg," unpublished research.
30. G. L. Makar, and J. Kreyer, "The Effect of Alloying Elements on the Corrosion Resistance of Rapidly Solidified Magnesium Alloys," to be published.
31. F. Sommer, Z. Metallkunde, Vol. 72, pp. 219-224, 1981.
32. F. Sommer, M. Fripan, and B. Predel in "Rapidly Quenched Metals," (RQ4) ed., T. Masumoto and K. Suzuki, The Japan Institute. Met. Sendai, pp. 209-212, 1982.
33. A. Calka, and H. Matyja, "Amorphous Metallic Materials," ed. P. Duhaj, and P. Mrafko, VEDA, Bratislava, pp. 71-82, 1980.

34. T. Matsuda, N. Shiotaniand, and U. Mizutani, J. Phys. F., Met. Phys., Vol. 14, pp. 1193-1204, 1984.
35. S. J. Poon, P. L. Dunn, and S. Smoith, J. Phys. F., Met. Phys., Vol. 12, pp. L101-6, 1982.
36. P. L. Dunn and S. J. Poon, *ibid*, pp. L273-8.
37. H. L. Lou, C. C. Chao, and P. Durvez, Trans. Met. Soc. AIME, Vol. 230, pp. 1488-1490, 1964.
38. G. L. Makar, and J. Kruger, presented at the 117th TMS Annual Meeting, Phoenix, AZ, 1988.
39. N. I. Vrich, and B. N. Latvin, Phys. Met. Metallogr., Vol. 16, No. 4, pp. 29-32, 1963.
40. M. C. Flemings, and A. Mortensen, "Rapid Solidification Processing of Magnesium Alloys," (Report AMMRC TR-84-37, U.S. Army Materials and Mechanics Research Center, Watertown, MA, Sept. 1984.
41. S. K. Das, C. F. Chang, and D. Raybould, Proceedings of 43rd Annual World Magnesium Conference (McLean, VA, International Magnesium Association, pp. 1-5, 1986.
42. K. Hasimoto, "Corrosion of Amorphous Alloys," in Structure and Properties of Amorphous Metals, eds., T. Masumoto and K. Suzuki, Suppl. Sc. Rep. RITU, Vol. A27, pp. 233-250, 1978.

APPENDIX 1

PUBLICATIONS LIST FOR THE AFOSR GRANT NO. AFOSR 85-0333

1. J. Mazumder and A. Kar, "Solid Solubility in Laser Cladding," J. Metals, Vol. 9, No. 2, pp. 18-23, 1987.
2. A. Kar and J. Mazumder, "One-dimensional Diffusion Model for Extended Solid Solution in Laser Cladding," J. Appl. Physics, Vol. 61, No. 7, pp. 2645-2655, 1987.
3. J. Singh and J. Mazumder, "Effect of Extended Solid Solution of Hf on the Microstructure of the Laser Clad Ni-Fe-Cr-Al-Hf Alloys," Acta Metallurgica, Vol. 35, No. 8, pp. 1995-2003, 1987.
4. J. Singh, K. Nagrathnam and J. Mazumder, "Oxidation Performance of Laser Clad Ni-Cr-Al-Hf Alloy on Inconel 718," Proc. of TMS-AIME High Temperature Coating Conf., Florida, pp. 101-112, M. Khobaib and R. C. Krutenat (Eds.), 1986.
5. J. Singh, K. Nagrathnam and J. Mazumder, "Laser Cladding of Ni-Cr-Al-Hf on Inconel 718 for Improved High Temperature Oxidation Resistance," High Temp. Technology Vol. 5, No. 3, pp. 131-136, August, 1987.
6. A. Kar and J. Mazumder, "One-dimensional Finite-medium Diffusion Model for Extended Solid Solution in Laser Cladding of Hf on Nickel," Acta Metallurgica, Vol. 36, No. 3, pp. 701-712, 1988.
7. J. Singh and J. Mazumder, "In Situ Formation of Ni-Cr-Al-Hf Alloy by Laser Cladding with Mixed Power Feed," Proc. of LIM-3, published by IFS Publications Ltd., 1986.
8. J. Mazumder, A. Kar and J. Singh, "Theoretical and Experimental Studies of Laser Cladding of Ni-Cr-Al-Hf Alloys with Extended Solid Solution of Hf," Proc. of LAMP-87, Osaka, Japan, May 1987.
9. J. Singh and J. Mazumder, "Microstructure of Laser Clad Ni-Cr-Al-Hf Alloy on a γ Strengthened Ni-Base Superalloy," accepted for publication Metallurgical Transactions.
10. A. Kar and J. Mazumder, "Model for Nonequilibrium Segregation during Rapid Solidification," submitted to Physical Review B.
11. A. Kar and J. Mazumder, "Extended Solid Solution and Nonequilibrium Phase Diagram for Ni-Al Alloy Formed during Laser Cladding," submitted to Met. Trans. A, Vol. 20A, p. 363-371, March, 1989.